Multi-scale modeling and simulation of low-pressure methane bi-reforming using structured catalytic reactors

Florent Minette[1,2] and Juray De Wilde[*1,2]

[1]UCLouvain, Institute of Mechanics, Materials & Civil Engineering (iMMC), Materials & Process Engineering (IMAP), 1348 Louvain-la-Neuve, Belgium

[2]UCLouvain, Research and Innovation Centre for Process Engineering (ReCIPE), 1348 Louvain-la-Neuve, Belgium

[*]Corresponding author: juray.dewilde@uclouvain.be

Abstract

Methane bi-reforming has gained interest recently for its potential of converting CH_4 and CO_2 into chemicals while avoiding catalyst deactivation by coke formation. Recycling CO_2 produced can be considered, but introduces constraints on the allowable pressure drop over the reactor. The latter is particularly the case in low-pressure processes, such as those encountered in the steel industry. The paper reports on a multi-scale modeling approach for a structured catalytic reactor that offers lower pressure drop than classical pellets while improving heat transfer. The use of a thin catalytic coating furthermore improves the catalyst effectiveness. The coupled CFD-reaction model accounts for the details of the reaction mechanism and kinetics, intra-catalyst transport and the details of the flow pattern. Radiative heat transfer and thermal conduction in the reactor tube walls and in the reactor internals coated with catalyst are also taken into account. Several scale-bridging strategies have to be introduced and combined to allow a computationally tractable solution. This requires a variety of detailed experimental data, an aspect that is also discussed. The coupled CFD-reaction model was first validated using data from a bi-reforming pilot plant and then used to evaluate the performance of a structured reactor under typical commercial process conditions and to study optimization of the reactor design and potential increase in capacity.

Keywords

- Multi-scale modeling
- Methane bi-reforming
- Structured catalytic reactors

1 Introduction

The availability of natural gas and concerns about global warming have led to growing interest in dry-reforming of methane. The process catalytically converts two major greenhouse gases (CH_4 and CO_2) into higher value chemicals [1, 2]. The process however faces challenges regarding rapid catalyst deactivation by coke deposition [3]. The combined steam and CO_2 reforming of methane, referred to as bi-reforming, has recently gained attention as an alternative for dry-reforming of methane. The addition of steam allows significantly reducing or eliminating coke formation and changing the H_2O/CO_2 feed ratio also allows adjusting the syngas H_2/CO-ratio [4, 5]. Several Ni-based catalysts were found to be highly active and selective for bi-reforming of methane [5–8]. The addition of promotors such as tin, cerium dioxide or boron was studied to reduce coke formation and allow operation at lower H_2O/CO_2-ratio [8–10].

Recycling exhaust CO_2 to the inlet of the reformer is possible but requires a low pressure drop over the reactor. This is particularly the case for low-pressure processes, such as developed for iron oxide reduction that operates the reformer at around 2 bar. In such processes, CO_2 and H_2O produced in the shaft furnace are recycled along with unreacted CO and H_2 to the inlet of the reformer (Figure 1). Operation in a closed loop system allows minimizing the natural gas and steam consumption and eliminating the need for an expensive CO_2 removal system. The major challenge for the reformer catalyst is to combine low pressure drop with efficient heat transfer. Methane bi-reforming is indeed strongly endothermic and the ability to supply sufficient heat while ensuring radial temperature uniformity and not exceeding the maximum tube skin temperature typically limits the capacity

of the reformer. This limits the diameter of the reactor tubes that are suspended in the reformer furnace and imposes constraints on the reformer catalyst size and shape. With conventional catalyst pellets, whatever their design, lower pressure drop implies less efficient heat transfer. Structured catalytic reactors have been recently developed for process intensification [11] and to offer lower pressure drop combined with more efficient heat transfer as compared to pellets. A thin catalyst coating is typically applied on the structure which also allows reducing intra-catalyst diffusion limitations that are strong with pellets [12]. 3D printing allows using shapes that are otherwise difficult to manufacture [13] but is so far relatively expensive. For intensified hydrogen production technologies, different manufactured designs have been tested at the lab, pilot and commercial scales, such as monolithic catalysts [14], conductive packed foam configurations [15], the Catacel™ reactor [16] and the annular ZoneFlow™ reactor [17, 18]. Improved heat management ability compared to conventional pellets was demonstrated. A ZoneFlow™ reactor consists of a central core with a specific conical collar design supporting a near-wall annular casing with a specific sector and blade design. By the action of the flow and its weight on the conical collars, the casing is pushed outward and good contact between the casing and the reactor tube wall is ensured. The annular casing has consecutive and interconnected sectors with blades guiding the flow towards and away from the wall (Figure 2). The blades make an angle with the reactor tube wall and radial fins separate the sectors except in the near-wall regions where openings allow flow. The net effect is flow impinging the tube wall and locally increased turbulence, i.e. in the near-wall regions, as a result of the strong gradients in the mean velocity field. This results in improved heat transfer between the tube wall and the process gas and reduced pressure drop.

Evaluating the performance of a reactor with a complex flow pattern requires the coupled simulation of the fluid dynamics and the reactions. This approach allows facilitating scale-up, studying details of the reactor design and obtaining information that is difficult or impossible to measure. In recent years, several groups successfully performed 3D resolved-particle fixed bed CFD simulations for methane steam or dry reforming [19–22]. Applying scale-bridging strategies at the different scales to account for detailed reaction mechanism and flow pattern helped obtaining insight and fundamental understanding of fixed bed reactors, such as local transport phenomena and intraparticle gradients limitations, influence of pellets shape and inclination and the importance of radiative heat transfer [23–27]. Several authors applied similar flow-reaction coupling approach for the 2D or 3D simulation of coated catalytic reactors [28–30]. CFD simulations on a specific ZoneFlow™ reactor design for SMR were performed by De Wilde and Froment (2012, 2013) [31, 32] to confirm efficient heat transfer and low pressure drop and to verify that, under typical commercial SMR conditions, the provided geometric surface area in combination with intensified heat transfer and high catalyst effectiveness factors allow a methane conversion comparable or higher than that achieved in a conventional packed bed, despite the relatively low amount of catalyst used. The simulations also showed that efficient heat transfer in the near-wall casing reduces the risk of hot spots, opening perspectives for operation at lower steam-to-carbon ratio, with reduced risk of coke formation.

The present work focuses on the evaluation of the performance of ZoneFlow™ structured reactors (Figure 2) for methane bi-reforming. Applying different scale-bridging strategies, a detailed multi-scale 3D steady-state CFD-reaction model is developed, accounting for the details of the reaction mechanism and the intrin-

sic reaction kinetics, intra-catalyst diffusion limitations, turbulence, radiative heat transfer and thermal conduction in the reactor tube walls and internals coated with catalysts. Pressure drop data from cold flow tests in a wide flow rate range are used to estimate the turbulence model parameters. Next, temperature and methane conversion data from bi-reforming pilot plant tests are used to validate the overall performance of the coupled CFD-reaction model. The latter is then used to simulate the performance of a commercial scale reactor under typical methane bi-reforming process conditions. Comparison with a conventional packed bed reactor is made and the differences in behavior are analyzed. Finally, considering hybrid ZoneFlow™ /packed bed reactors, reactor design optimization is addressed and potential capacity increase evaluated.

2 Multi-scale modeling approach

Figure 3 summarizes the multi-scale modeling approach and scale-bridging strategies that are used. For the reaction rates, scale bridging is achieved by applying the rate determining step theory and using intrinsic kinetics per unit mass of catalyst coating. As a results, rate expressions and rate parameters are catalyst dependent and to be determined experimentally or calculated theoretically [33–36]. To account for intra-catalyst transport and reaction, a pseudo-continuum description of the catalyst is used. This allows a 1D intra-catalyst calculation, but introduces catalyst dependent model parameters - the catalyst porosity and tortuosity - to be measured experimentally or estimated theoretically [37]. To account for the complex flow in the reactor, a Computational Fluid Dynamics (CFD) approach is used. Calculating the details of turbulence and boundary layers at solid walls requires extremely fine meshes and transient simulations, computationally not tractable for the

simulation of commercial scale reactors. A common scale-bridging strategy is to average the Navier-Stokes equations over all scales of turbulence and solve the so-called Reynolds-Averaged Navier-Stokes (RANS) equations. To close the RANS equations, effective transport properties can be introduced, that are to be calculated through a turbulence model [38, 39]. Wall functions are used to prevent explicit calculation of the near-wall boundary layers. Different turbulence models have been proposed and selection of the appropriate model is not always evident. Furthermore, turbulence model parameters are introduced, to be determined from Direct Numerical Simulations (DNS) or from dedicated experiments. Details on the catalyst and intrinsic kinetics are given in Section 2.1. The calculation of the intra-catalyst behavior is discussed in Section 2.2. Finally, the CFD approach is presented in Section 2.3.

2.1 Catalyst and intrinsic reaction kinetics

Figure 4 shows a SEM picture of the Alloys Surfaces Co., Inc. (ASC) metal structure with a thin, nanostructured and adherent Ni coating that was used in the bi-reforming pilot plant tests and reactor simulations. The process developed by ASC ensures integral bonding of the nanostructured catalytic layers [40]. The material can be used as a catalyst or catalyst support and in various forms (foil, fiber, mesh or tube). The mechanical robustness allows forming the structure of the reactor internals using the material as such, that is, after coating. The absence of delamination under severe process conditions and the potential to replace wash-coated layers were demonstrated [40]. For the pilot plant tests and simulations, a 100 μm support with a 10 μm Ni catalyst layer on each side was used.

The catalytic conversion of methane with steam and CO_2 proceeds through the set of elementary steps shown in Figure 5. These are captured by three global

reactions, two steam methane reforming (SMR) reactions and the Water-Gas Shift (WGS) reaction:

$$CH_4 + H_2O \rightleftharpoons CO + 3H_2 \quad \text{(I)}$$

$$CO + H_2O \rightleftharpoons CO_2 + H_2 \quad \text{(II)}$$

$$CH_4 + 2H_2O \rightleftharpoons CO_2 + 4H_2 \quad \text{(III)}$$

As suggested by Donazzi et al. (2008) [41], the specific CO_2-reforming reaction can be excluded. The intrinsic kinetics of the two SMR reactions on the Ni-based ASC catalyst was previously studied [42, 43] and determined from measurements in a specifically designed experimental reactor. The kinetic modeling confirmed the reaction mechanism identified by Xu and Froment (1989) [44] with a different rate determining step for the second SMR reaction (Figure 5), leading to the following rate expressions:

$$r_I = \frac{\dfrac{k_I}{p_{H_2}^{2.5}}\left(p_{CH_4}p_{H_2O} - \dfrac{p_{CO}p_{H_2}^3}{K_I}\right)}{\text{DEN}^2} \quad (1)$$

$$r_{II} = \frac{\dfrac{k_{II}}{p_{H_2}}\left(p_{CO}p_{H_2O} - \dfrac{p_{CO_2}p_{H_2}}{K_{II}}\right)}{\text{DEN}^2} \quad (2)$$

$$r_{III} = \frac{\dfrac{k_{III}}{p_{H_2}^2 p_{H_2O}}\left(p_{CH_4}p_{H_2O}^2 - \dfrac{p_{CO_2}p_{H_2}^4}{K_{III}}\right)}{\text{DEN}^2} \quad (3)$$

with the denominator, common for the three reactions, given by:

$$\text{DEN} = 1 + K_{CH_4}p_{CH_4} + K_{CO}p_{CO} + K_{H_2}p_{H_2} + K_{H_2O}\frac{p_{H_2O}}{p_{H_2}} \quad (4)$$

The catalyst specific rate parameters that were estimated are summarized in Table 1, for partial pressures expressed in bar and reaction rates in mol/kg_{cat}.h. Compared to the conventional SMR catalyst studied by Xu and Froment (1989) [44], the ASC catalyst was found to be less active for the first SMR reaction, but more active for the second SMR reaction. The rate determining steps theory on which the Langmuir-Hinshelwood-Hougen-Watson type rate expressions are based is essential for scale-bridging. The details of the reaction mechanism, rate determining steps and the equilibria of the non-rate determining steps are accounted for in rate expressions that can be easily implemented in the catalyst/reactor model.

The mechanism of coke formation is also included in Figure 5. Snoeck et al. [45–48] studied the initial coke formation on a conventional SMR catalyst and derived rate expressions that allow verifying if net positive coke formation is to be feared. The global C-formation reactions to be considered are:

$$CH_4 \rightleftharpoons C + 2H_2 \tag{C-1}$$

$$CO{+}H_2 \rightleftharpoons C + H_2O \tag{C-2}$$

The Langmuir-Hinshelwood-Hougen-Watson type rate expressions were adopted from Snoeck et al. [45–48] and are given by:

$$r_{C1} = \frac{k_M^+ \, \widetilde{K}_{CH_4} \left(p_{CH_4} - \dfrac{p_{H_2}^2}{K_M^*} \right)}{\mathrm{DEN}2^2} \tag{5}$$

$$r_{C2} = \frac{\left(k_O^- K_{CO} p_{CO} - \dfrac{k_O^{+'}}{K_{O,H_2O}} \dfrac{p_{H_2O}}{p_{H_2}} \right)}{\mathrm{DEN}2^2} \tag{6}$$

with the denominator:

$$\text{DEN2} = 1 + K_{CO} p_{CO} + \widetilde{K}_{CH_4}\, p_{CH_4} + \frac{1}{K_r''} p_{H_2}^{1.5} + \frac{1}{K_{O,H_2O}} \frac{p_{H_2O}}{p_{H_2}} \tag{7}$$

The rate parameters are also given in Table 1, for partial pressures expressed in bar and coking reaction rates expressed in kmol/m_i^2.h. As coke formation is typically to be prevented, the coke formation analysis is carried out *a posteriori*, that is, using the temperature and species concentration profiles that follow from the reactor simulation with a coke-free catalyst.

2.2 Intra-catalyst transport

Despite the small catalyst layer thickness (10 μm), the catalyst internal structure with in particular its low porosity can cause intra-catalyst diffusion limitations under typical commercial process conditions. The typically used scale-bridging strategy is to describe the catalyst as a continuum, introducing effective diffusivities that depend on the catalyst porosity, ε_s, and tortuosity, τ, two parameters to be determined experimentally or through detailed pore structure models [49]:

$$\mathcal{D}_{e,A} = \frac{\varepsilon_s}{\tau} \left(\frac{1}{\mathcal{D}_{Am}} + \frac{1}{\mathcal{D}_{AK}} \right)^{-1} \tag{8}$$

with $\mathcal{D}_{AK}$ the Kudsen diffusivity and $\mathcal{D}_{Am}$ the molecular diffusivity, the latter being calculated with the semi-empirical relation of Fuller-Schettler-Giddings [49]. The BET surface area, catalyst porosity and pore size distribution were measured by nitrogen adsorption-desorption [42]. The porosity of the coating, ε_s, was found to be 0.084, which is small compared to that of conventional catalyst and is the result of the coating technique developed by ASC to ensure a good coating adherence and resistance to delamination [40, 42, 43]. The BET surface area was found to be

7.4 m^2/g_{cat}. In comparison, a conventional SMR catalyst has a BET surface area of around 58 m^2/g_{cat} with a Ni surface area of around 9.3 m^2/g_{cat} [44]. The difference in composition and density of the conventional and ASC catalyst should, however, be accounted for. Whereas the former consists of Ni dispersed on a Mg/Al_2O_4 spinel support, the latter is a nearly pure Ni layer. Figure 6 shows the tortuosity, τ, estimated using reported correlations [37, 50–54]. A value of 4 was used for the simulations, best in line with the value of τ reported by Xu and Froment [12,44] for the conventional SMR catalyst ($\varepsilon_s = 0.528$ and $\tau = 3.54$).

The intra-catalyst species concentration profiles can then be calculated from the species continuity equations inside the catalyst:

$$-\frac{d}{d\zeta}\left(\mathcal{D}_{e,A}\frac{dC_{A,s}}{d\zeta}\right) = \rho_s \sum_k \alpha_{Ak} r_k \left(\boldsymbol{C_s}, T_s\right) \tag{9}$$

with boundary conditions:

$$\text{at } \zeta = \frac{d_{\text{struc}}}{2} \qquad -\mathcal{D}_{e,A}\frac{dC_{A,s}}{d\zeta}\bigg|_{\zeta=d_{\text{struc}}/2} = k_g\left(C^s_{A,s} - C_A\right) \tag{10}$$

$$\text{at } \zeta = \frac{d_{\text{sup}}}{2} \qquad -\mathcal{D}_{e,A}\frac{dC_{A,s}}{d\zeta}\bigg|_{\zeta=d_{\text{sup}}/2} = 0 \tag{11}$$

The solid internals of thickness d_{struc} consist of a support of thickness d_{sup} and on both sides a catalyst layer of thickness d_{cat}, so that $d_{\text{struc}} = d_{\text{sup}} + 2d_{\text{cat}}$ and $f_{\text{struc,cat}} = 2d_{\text{cat}}/(d_{\text{sup}} + 2d_{\text{cat}})$. In the CFD reactor model, intra-catalyst diffusion limitations are accounted for using catalyst effectiveness factors, η_k. The latter can be rigorously calculated by solving the species continuity equations 9-11 inside the

catalyst layer [49], with:

$$\eta_k = \frac{\int_{d_{\text{sup}}/2}^{d_{\text{struct}}/2} \frac{r_k(C_{As})}{r_k(C_{As}^s)} d\zeta}{\left(\frac{d_{\text{struct}}}{2} - \frac{d_{\text{sup}}}{2} \right)} \tag{12}$$

The solid phase species continuity equations 9 and corresponding boundary conditions can then be integrated in the CFD simulations using the following algebraic equations:

$$k_g \left(C_{As}^s - C_A \right) = \rho_s d_{\text{cat}} \sum_k \alpha_{Ak} \eta_k r_k \left(\boldsymbol{C_s^s}, T_s \right) \tag{13}$$

To reduce the calculation time, the catalyst effectiveness factors can eventually be independently estimated for the typical operating conditions encountered in the reactor and then be used as such in the CFD-reaction simulation, as in [31, 32]. Figure 7 shows intra-catalyst species concentration profiles for a 10 μm catalyst layer thickness, at typical low-pressure bi-reforming process conditions (Ts = 1023 K, P = 2 bar, $y_{CH_4} = 0.15$, $y_{H_2O} = 0.125$, $y_{H_2} = 0.375$, $y_{CO} = 0.205$, $y_{CO_2} = 0.14$). Catalyst effectiveness factors close to one are observed for the two steam reforming reactions, despite the low catalyst porosity. The influence of the catalyst layer thickness was discussed in [42]. For comparison, with conventional catalyst pellets under commercial SMR conditions, the catalyst effectiveness factors for the two steam reforming reactions are much smaller, of the order 0.02-0.05, but also relatively constant in most of the reactor [12].

Accounting for thermal conduction in the solid internals coated with catalyst, the temperature of the solid internals is calculated from:

$$-\frac{\partial}{\partial \zeta} \lambda_s \frac{\partial T_s}{\partial \zeta} = f_{\text{struct,cat}} \rho_s \sum_k \eta_k r_k \left(\boldsymbol{C_s}, T_s \right) \left(-\Delta H \right)_k \tag{14}$$

where λ_s is the thermal conductivity of the solid internals. At the boundary with the process gas:

$$\text{at } \zeta = \frac{d_{\text{struct}}}{2} \qquad -\lambda_s \left.\frac{dT_s}{d\zeta}\right|_{\zeta = d_{\text{struct}}/2} = h_f \left(T_s^s - T_g\right) \tag{15}$$

and at the boundary between the two sides of the support:

$$\text{at } \zeta = 0 \qquad -\lambda_s \left.\frac{dT_s}{d\zeta}\right|_{\zeta=0}^{\text{side 1}} = \left.\frac{dT_s}{d\zeta}\right|_{\zeta=0}^{\text{side 2}} = 0 \tag{16}$$

The calculation of k_g and h_f, the effective coefficients of mass and heat transfer between the solid internals coated with catalyst and the process gas, requires information on the flow pattern in the reactor and is dealt with in a next section.

2.3 CFD reactor model

First the 3D CFD model to account for the complex flow in ZoneFlow™ reactors is presented. The 1D model used for the simulation of the reference packed bed reactor is briefly described at the end of this section. Explicit simulation of the details of turbulence requires solution of the transient Navier-Stokes equations and use of extremely fine spatial and temporal meshes. In most cases, interest goes to the statistically stationary reactor performance. To reduce the calculation time, the Reynolds-Averaged Navier-Stokes (RANS) approach is adopted, averaging the Navier-Stokes equations over all scales of turbulence to calculate the Reynolds-averaged variables. Averaging non-linear terms introduces additional terms in the RANS equations that describe the influence of turbulence on the evolution of the Reynolds-averaged variables and creates a scale-bridging or so-called closure problem. The most widely used closure models are based on the introduction of effective

transport properties - viscosity, conductivity and diffusivity. With that and using the Einstein notation and Reynolds-averaged variables, the transport or continuity equations can be written:

Gas phase total continuity equation:

$$\frac{\partial\left(\rho_g u_j\right)}{\partial x_j} = 0 \tag{17}$$

Gas phase momentum equations:

$$\frac{\partial\left(\rho_g u_i u_j\right)}{\partial x_j} = -\frac{\partial P_e}{\partial x_i} + \frac{\partial \tau_{ij}}{\partial x_j} + \rho_g g_i \tag{18}$$

Gas phase energy equation:

$$\frac{\partial\left(\rho_g E_g u_j\right)}{\partial x_j} - \frac{\partial}{\partial x_j}\left(\lambda_e \frac{\partial T_g}{\partial x_j}\right) = -\frac{\partial\left(P_e u_j\right)}{\partial x_j} + \frac{\partial\left(u_i \tau_{ij}\right)}{\partial x_j} + \rho_g g_j u_j \tag{19}$$

Gas phase species continuity equations:

$$\frac{\partial\left(C_A u_j\right)}{\partial x_j} = \frac{\partial}{\partial x_j}\left(D_{A,e} \frac{\partial C_A}{\partial x_j}\right) \tag{20}$$

Calculating the tube wall temperatures requires accounting for thermal conduction in the reactor tube:

$$-\lambda_{\text{tube}}\left(\frac{\partial^2 T_{\text{tube}}}{\partial r^2} + \frac{1}{r}\frac{\partial T_{\text{tube}}}{\partial r}\right) - \lambda_{\text{tube}}\frac{\partial^2 T_{\text{tube}}}{\partial x^2} = 0 \tag{21}$$

The gas phase shear stress tensor in Equations 18-19 is defined as:

$$\tau_{ij} = \mu_e\left[\left(\frac{\partial u_i}{\partial x_j} + \frac{\partial u_j}{\partial x_i}\right) - \frac{2}{3}\delta_{ij}\frac{\partial u_k}{\partial x_k}\right] \tag{22}$$

The effective mean pressure, effective viscosity, effective conductivity and effective diffusivity that are introduced in Equations 18-20 and 22 consist of a molecular and turbulent contribution:

$$P_e = P + \frac{2}{3}\rho_g k \tag{23}$$

$$\mu_e = \mu_g + \mu_t \tag{24}$$

$$\lambda_e = \lambda_g + \lambda_t + \lambda_r \tag{25}$$

$$D_{A,e} = D_{A,m} + D_t \tag{26}$$

The effective conductivity (25) accounts for radiative heat transfer also, as discussed hereafter. The calculation of these effective transport properties requires information on the turbulence. Various turbulence models have been developed and considered in this study. The two-equation $k - \epsilon$ model is selected, with k the turbulent kinetic energy and ϵ the turbulence dissipation rate. The turbulent viscosity can be calculated from k and ϵ as [38, 39]:

$$\mu_t = C_\mu \rho_g \frac{k^2}{\epsilon} \tag{27}$$

with C_μ a turbulence model parameter that was determined for a variety of flows. Based on the similarity between mass, heat and momentum transfer, the turbulent conductivity and diffusivity are related to the turbulent viscosity:

$$\lambda_t = \frac{c_p \mu_t}{Pr_t} \tag{28}$$

$$D_t = \frac{\mu_t}{\rho_g Sc_t} \tag{29}$$

Pr_t , the turbulent Prandtl number, has a typical value of 0.85. The turbulent Schmidt number, Sc_t, has a typical value of 0.7. The turbulent kinetic energy and its dissipation rate are required to calculate the turbulent viscosity (Equation 27) and from that the turbulent conductivity (Equation 28) and diffusivity (Equation 29).

The standard $k-\epsilon$ model is used. The transport equation for k is:

$$\frac{\partial\left(\rho_g k\langle u_i\rangle\right)}{\partial x_i}=\frac{\partial}{\partial x_i}\left[\left(\mu_g+\frac{\mu_t}{\sigma_k}\right)\frac{\partial k}{\partial x_i}\right]+G_k+G_b-\rho_g\epsilon \tag{30}$$

where σ_k is the turbulent Prandtl number for k, a model parameter with typical value of 1.0, G_k is the turbulent kinetic energy generation due to the mean velocity gradients and G_b is the turbulent kinetic energy generation due to buoyancy:

$$G_k=-\rho_g\langle u_i' u_j'\rangle\frac{\partial u_j}{\partial x_i} \tag{31}$$

$$G_b=\beta g_i\frac{\mu_t}{Pr_t}\frac{\partial T_g}{\partial x_i} \tag{32}$$

with β the thermal expansion coefficient:

$$\beta=-\frac{1}{\rho_g}\left(\frac{\partial\rho_g}{\partial T_g}\right)_P \tag{33}$$

The semi-empirical transport equation for ϵ is:

$$\frac{\partial\rho_g\epsilon\langle u_i\rangle}{\partial x_i}=\frac{\partial}{\partial x_i}\left[\left(\mu_g+\frac{\mu_t}{\sigma_\epsilon}\right)\frac{\partial\epsilon}{\partial x_i}\right]+C_{\epsilon1}\frac{\epsilon}{k}\left(G_k+C_{\epsilon3}G_b\right)-C_{\epsilon2}\rho_g\frac{\epsilon^2}{k} \tag{34}$$

where σ_ϵ is the Prandtl number for ϵ, with typical value of 1.3. The standard $k-\epsilon$ model is robust and offers a reasonable accuracy for a wide range of turbulent flows. $C_{\epsilon1}$ and $C_{\epsilon2}$ are the model parameters which were determined from experimental data for a variety of flows [38, 39]. As discussed in the next section, the values of the turbulence model parameters found in the literature may not be applicable and need to be re-estimated from experimental measurements.

To describe the radiative heat transfer, the Rosseland or diffusion approximation is adopted. The latter assumes that the radiation intensity is the black-body intensity

at the gas temperature. The use of the Rosseland radiation model can be justified by the presence of steam and carbon dioxide in the reaction mixture, absorbing radiation. Linearization of the radiative heat flux in a gray medium results in:

$$\lambda_r = \frac{16\sigma n^2 T_g^3}{3(a+\sigma_s) - C\sigma_s} \tag{35}$$

where n is the refractive index. The so-called radiative conductivity λ_r is expressed as a function of an absorption coefficient a and a scattering coefficient σ_s, describing the change in radiation intensity per unit length along the path through the fluid medium. A gray radiation model is used assuming that the absorption coefficient a is band independent. The absorption coefficient is then calculated as a function of local concentrations of H_2O and CO_2, using the Weighted Sum of Gray Gases Model (WSGGM) [55,56]. The Rosseland model does not solve an extra transport equation, which makes it very convenient for commercial scale simulations. Alternatively, the Discrete Ordinate (DO) model can be used, accounting for surface radiation and participating media effects. The radiative transfer equation (RTE) is solved in a finite number of discrete solid angles, s_i:

$$\frac{\partial I_{si}(r,s)}{\partial x_i} + (a+\sigma_s)I(r,s) = an^2\frac{\sigma T^4}{\pi} + \frac{\sigma_s}{4\pi}\int_0^{4\pi} I(r,s')\Phi(s.s')d\Omega' \tag{36}$$

Each octant 4π of the angular space is discretized into $N_\theta \times N_\phi$ solid angles at any spatial location, θ and ϕ being the polar and azimuthal angles, respectively. In this study N_θ and N_ϕ have been imposed to 3, leading to a total of 72 directions solved. This makes the DO model considerably more expensive in terms of calculation time, compared to the Rosseland model.

Equations 17-19 have to be solved with the appropriate boundary conditions. For the momentum equation 18, the no-slip condition is applied at solid walls.

The wall shear stress is calculated from the logarithmic law [57], valid for $y^* = \rho C_\mu^{1/4} k^{1/2} y_1/\mu \geqslant 11.225$:

$$U^* = \frac{\langle u \rangle \rho C_\mu^{1/4} k^{1/2}}{\tau_w} = \frac{1}{\kappa} \ln\left(y^* C_E\right) \tag{37}$$

where y^* is the distance to the wall, C_E an empirical constant with value 9.793 and κ the von Karman constant with value 0.42. If the mesh is sufficiently fine, such as $y^* < 11.225$, the laminar stress-strain relationship is applied at the wall-adjacent cells, so that:

$$U^* = y^* \tag{38}$$

For the energy equations 19 and 21, at the reactor tube inner and outer wall:

$$r = d_{\text{tube}}^{\text{in}}: \qquad -\lambda_{\text{tube}} \left.\frac{\partial T_{\text{w}}}{\partial r}\right|_{r=d_{\text{tube}}^{\text{in}}} = \alpha^{\text{in}} \left(T_g - T_{\text{w,in}}\right) \tag{39}$$

$$r = d_{\text{tube}}^{\text{out}}: \qquad -\lambda_{\text{tube}} \left.\frac{\partial T_{\text{w}}}{\partial r}\right|_{r=d_{\text{tube}}^{\text{out}}} = \alpha^{\text{out}} \left(T_{\text{w,out}} - T_{\text{furnace}}\right) \tag{40}$$

in which α^{in} and α^{out} are the effective coefficients of heat transfer between the inner wall of the reactor tube and the process gas and between the outer wall of the reactor tube and the furnace respectively. Convection and radiation are accounted for, with a temperature boundary condition for the radiative heat flux at the furnace side. The boundary conditions at solid internals were given in Section 2.2. For the calculation of h_f in Equation 15 and α_i in Equation 39, the model of Jayatilleke (1969) is applied [58]:

$$\text{for } y^* < y_T^* \qquad h_f \text{ or } \alpha_i = \frac{\rho_g c_p C_\mu^{1/4} k^{1/2}}{Pr\, y^*} \tag{41}$$

$$\text{for } y^* \geq y_T^* \qquad h_f \text{ or } \alpha_i = \frac{\rho_g c_p C_\mu^{1/4} k^{1/2}}{Pr_t \left[\dfrac{1}{\kappa} \ln\left(y^* C_E\right) + P_T \right]} \tag{42}$$

with

$$P_T = 9.24 \left[\left(\frac{Pr}{Pr_t} \right)^{0.75} - 1 \right] \left[1 + 0.28 \exp\left(-\frac{0.007 Pr}{Pr_t} \right) \right] \tag{43}$$

and y_T^* the non-dimensional thermal sub-layer thickness determined by the intersection of the linear and logarithmic laws. The mass transfer coefficient k_g in Equation 13 is calculated in a similar way:

$$\text{for } y^* < y_C^* \qquad k_g = \frac{\rho_g c_p C_\mu^{1/4} k^{1/2}}{Sc\, y^*} \tag{44}$$

$$\text{for } y^* \geq y_C^* \qquad k_g = \frac{\rho_g C_\mu^{1/4} k^{1/2}}{Sc_t \left[\dfrac{1}{\kappa} \ln\left(y^* C_E\right) + P_C \right]} \tag{45}$$

where y_C^* is similarly determined by the intersection of the linear and logarithmic laws and with

$$P_C = 9.24 \left[\left(\frac{Sc}{Sc_t} \right)^{0.75} - 1 \right] \left[1 + 0.28 \exp\left(-\frac{0.007 Sc}{Sc_t} \right) \right] \tag{46}$$

The $k - \epsilon$ turbulence model equations 30-34 cannot be applied in the viscous sub-layer near solid walls. Wall functions are used for the logarithmic layer:

$$k_w = \frac{u_\tau^2}{C_\mu^{1/2}} \tag{47}$$

$$\epsilon_w = \frac{u_\tau^4}{50\kappa\nu} = \frac{u_\tau^3}{\kappa y_1} \tag{48}$$

where $u_\tau = (\tau_w/\rho_g)^{1/2}$.

When the DO model is used to describe radiative heat transfer, the reactor tube wall and the ZoneFlow™ structure are treated as opaque walls. The heat flux emitted from a wall surface at temperature T_w is given by $n^2\epsilon_w\sigma T_w^4$, where ϵ_w is the wall emissivity, a material properties. Given q_{in}, the radiative incident heat flux on the wall, the amount of energy absorbed is calculated by $\epsilon_w q_{in}$ and the amount of energy reflected is calculated by $(1-\epsilon_w)q_{in}$. In this study, it is assumed that the energy is exclusively reflected diffusely. The emissivity of the reactor tube wall (inconel) is set to 0.95 and the emissivity of the blades coated with the Ni-based catalyst is set to 0.25, typically reported values.

The set of partial differential and algebraic equations were integrated with the finite volume solver Fluent 18.1 (Ansys). A second-order upwind scheme is used for the convective fluxes and the equations are solved by means of the SIMPLE algorithm for the pressure-velocity coupling. The low-Mach number assumption is used and the ideal gas law is adopted to account for density variations by temperature, pressure and composition fluctuations. The reactor can be simulated imposing the tube skin temperature profile or the furnace temperature. In the latter case, a furnace model accounting for convection and radiation is coupled with the CFD-reaction model.

For the simulation of a conventional packed bed, a 1D heterogeneous reactor model accounting for interfacial and intra-particle transport limitations was used [49]. The pressure drop was evaluated using the Ergun equation [59]. The wall-process gas heat transfer coefficient was calculated using the correlation of de Wasch and Froment [60]. The set of differential and algebraic equations was solved using Matlab. A 4^{th} order Runge-Kutta routine was combined with a finite difference method for the integration of the intra-particle species continuity equations.

3 Parameter estimation and model validation using pilot plant data

3.1 Reactor geometry and operating conditions

The cold flow pressure drop and low-pressure bi-reforming pilot plant tests were carried out with the ZoneFlow™ reactor shown in Figure 2(a). The blades in the different sectors guide the flow towards and away from the wall. The radial fins between the sectors provide a gap for flow between the sectors in the near-tube and near-central rod wall regions. Note that the reactor was operated with up-flow, down-flow being also possible. The generated geometry used for the CFD simulations is shown in Figure 2(b). To reduce the computational cost, a 38° sector of the reactor containing 2 centrifugal and 2 centripetal blades sectors is simulated and rotational periodic boundary conditions are applied. Several mesh refinement steps were necessary to ensure a grid independent solution, especially in the near-wall regions. The final mesh consists of 2.2 million cells and is illustrated in Figure 2(c).

Cold flow pressure drop measurements were taken at atmospheric pressure with air flow rates between 187 and 475 Nm^3/h, corresponding to superficial gas velocities between 2 and 5.3 $m_g^3/m_r^2.s$. The effective reactor tube diameter or channel width based Reynolds numbers is between ca. 4900 and 13000 and the sector width based Reynolds number between ca. 2400 and 6400. The flow is expected to be strongly turbulent in the near tube and near central rod wall regions, where gradients in the flow field are strong by the abrupt changes in velocity magnitude and direction in between sectors.

For the low-pressure bi-reforming pilot plant tests, the feed, a mixture of fresh feed and recycle streams, was preheated to 883 K and had a composition close to a typical commercial feed composition - see Table 2. The reactor outlet pressure was 2.5 bar. Two tests were carried out with feed flow rates of respectively 36.9 and 60.6 Nm^3/h. Channel width based Reynolds numbers are respectively 925 and 1515, sector width based Reynolds numbers 454 and 744, so that the flow is expected to be mainly laminar. The furnace temperature was around 1323 K and adjusted to guarantee a target gas outlet temperature of 1173 K, with actual values of respectively 1169 K and 1170 K.

3.2 Estimation of the turbulence model parameters by means of cold flow pressure drop data

The cold flow pressure drop tests were simulated using various turbulence models, including the standard and realizable k-ϵ models and the shear-stress transport (SST) k-ω model. Using the standard turbulence models parameters reported in the literature, and strictly only valid for given standard flows [39], none of these

models could accurately predict the measured pressure drop through the ZoneFlow™ reactor, as shown in Figure 8. Because of the relatively small differences in pressure drop predictions between the different turbulence models and the limited amount of data available to re-estimate the turbulence model parameters, the standard k-ϵ model was selected to verify if a good fit with the pressure drop measurements could be obtained with optimized parameters values. The two parameters, $C_{\epsilon 1}$ and $C_{\epsilon 2}$, in the semi-empirical ϵ-equation 34 were then optimized.

Figure 9 shows, for two applied gas flow rates (238 and 475 Nm^3/h), profiles of the pressure, velocity magnitude and turbulent kinetic energy in a cross section in the axial direction in a sector with blades guiding the flow away from the tube wall. The pressure profiles in Figure 9 confirm pressure drop in the flow direction inside the channels (in between two blades) is minimal and pressure drop is mainly generated by the flow in between sectors or channels, that is, in the near tube or near central rod wall regions. The abrupt changes in velocity magnitude and direction and related increased turbulence in these regions are responsible for the pressure drop and efficient heat transfer between the reactor tube wall and the process gas. The combination of improved heat transfer and low pressure drop of ZoneFlow™ reactors compared to conventional pellets is explained by this localized generation of turbulence and related pressure drop. A qualitatively similar behavior is observed in the entire flow rate range studied. Figure 8 shows that the CFD model is capable of predicting the observed relation between the gas flow rate and the pressure drop, provided that the turbulence model parameters are adjusted. The influence of the surface roughness factor on the pressure drop was found negligible. The pressure drop is seen to increase with the gas velocity to a power between 1 and 2, confirming the simultaneous presence of less and fully turbulent flow regions in the ZoneFlow™

reactors.

Figure 8 also shows cold flow pressure drop data for the identical diameter reactor tube packed with conventional pellets. For a low-pressure bi-reforming process, multi-holes reference pellets are 1.29 cm in equivalent diameter, defined as the diameter of the sphere with identical surface area per unit volume. With a typical bed void fraction of 0.56, the Ergun equation predicts well the pellets pressure drop data. The data confirm that the ZoneFlow™ reactor offers significantly lower pressure drop than the pellets.

3.3 CFD-reaction model validation by means of low-pressure methane bi-reforming pilot plant tests

Figures 10 shows simulations of low-pressure methane bi-reforming pilot plant tests using the CFD-reaction model without adjusting any of the independently determined transport or rate parameters and using the Rosseland model to describe radiative heat transfer. For the two pilot plant tests, contour plots of the axial velocity, gas phase and catalyst temperature and the CH_4 mole fraction in the gas phase and at the catalyst surface are shown. A qualitatively similar behavior is seen in the two tests. The axial velocity gradually increases as a result of the decreasing gas density. High velocities and high gradients in the velocity field are observed in the near-wall regions where the gaps that connect the different sectors are located. This can lead to local generation of turbulence, despite operation at low Reynolds number. As expected, strong differences in temperature between the process gas and reactor tube wall are observed. Even at the low gas flow rates used in the pilot plant tests, the temperature in a channel (between two blades) is relatively uniform, illustrating

efficient heat transfer. The differences in species concentrations between the process gas and the surface of the blades coated with catalyst are, however, also significant (1-6% in CH4 mole fraction). The consumption of methane by the reactions in the catalyst cannot be compensated for by interfacial mass transfer, intrinsically slow at the applied low flow rates. The differences in temperature between the gas phase and the surface of the blades are seen to be much less significant. This is due to significant contribution of radiative heat exchange in the ZoneFlow™ reactor at the applied operating temperatures.

Figure 11 and Table 3 compare the pilot plant measurements and CFD-reaction model predictions, using both the Rosseland and the DO model to describe radiative heat transfer. Figure 11(a)-(b) shows the gas and tube skin temperature profiles, Figure 11(c)-(d) and Table 3 the outlet concentrations of the dry gas and Figure 11(e)-(f) the simulated axial species concentrations profiles. The equilibrium gas composition at the measured exit temperature is also given in Table 3, indicating that equilibrium is not reached during the pilot plant tests. Simulations excluding thermal conduction in the reactor internals and/or radiative heat transfer (Table 3) show that with the considered support and catalyst layer thickness and high reactor void fraction, thermal conduction in the reactor internals has a minor contribution to the overall heat transfer, confirming the assumption of De Wilde and Froment [31,32]. The contribution of radiative heat transfer is, however, important and is essential to explain the fast increase of the temperature observed in the pilot plant tests. It can be seen that the outlet concentrations are accurately predicted using both radiation models. However, the DO model is not able to capture the rapid temperature increase experimentally observed, and the process gas temperature is generally under-predicted by this model (see Figure 11(c)-(d)). Therefore

the computationally less expensive Rosseland model was selected for the commercial scale simulations. Whereas the outlet concentrations and gas temperature profiles are accurately predicted with the Rosseland model, the outer wall temperature is slightly under-predicted. The latter can be explained by the way the tube skin temperature is measured. Probes containing a thermocouple are attached to the reactor wall (furnace side). A spring ensures contacting of the thermocouple with the wall, but because of the steep temperature gradient in the near-wall region, a 10-20 K error on the temperature measurement is easily possible. In some experiments, tube skin temperatures higher than the reported furnace box temperature were also recorded, which is physically impossible and confirms the order of the error on the wall temperature measurements.

As discussed in Section 2.2, in order to reduce calculation time, catalyst effectiveness factors were independently estimated for the typical operating conditions applied in the pilot plant tests and imposed as such in the CFD simulations. For validation, the 3D profiles of the effectiveness factors for the three global reactions were calculated *a posteriori*, using the temperature and species concentration profiles following from the reactor simulation. In the two pilot plant tests, the catalyst effectiveness factor of the first SMR reaction varied between 0.87 and 0.96 compared to the assumed constant value of 0.933, the effectiveness factor of the WGS reaction varied between 0.46 and 0.58 compared to the assumed constant value of 0.533 and the effectiveness factor of the second SMR reaction varied between 0.88 and 0.98, compared to the assumed constant value of 0.949. A maximum deviation of 0.073 on the constant value imposed for effectiveness factors was as such revealed.

In Section 4, simulations at typical commercial scale process conditions are presented to evaluate the contribution of radiative heat transfer and transport limitations under such conditions.

4 Commercial scale reactor simulations

4.1 Reactor geometry and operating conditions

A typical commercial scale low-pressure bi-reformer is simulated using the CFD-reaction model. The ZoneFlow™ design is identical to the one used in the pilot plant tests described in the previous section. The commercial scale reactor has the same diameter than the pilot plant reactor, but is 15 times longer. Simulations are first carried out with a typical feed rate of 399 Nm^3/h of mixed fresh and recycle gas per tube (see Figure 1), preheated at 853.15 K. The channel width based Reynolds number is then 9600-12900, the sector width based Reynolds number 4700-6300. The mixed feed gas composition is reported in Table 2. The simulations use an imposed constant furnace temperature of 1323 K. The reactor outlet pressure is 2 bar. A comparison with the performance of a conventional packed bed reactor is made imposing equal reaction kinetics, as determined for the ASC catalyst. A hybrid reactor design combining the ZoneFlow™ reactor with the conventional pellets is then considered to study potential capacity increase. The results are summarized in Table 4.

4.2 ZoneFlow™ reactor performance

The qualitative picture observed in the pilot plant tests is confirmed at typical commercial conditions. Turbulence is, however, significantly more pronounced, es-

pecially in the near-reactor tube and near-central rod wall regions. Figure 12 shows profiles of (a) methane mole fraction, (b) tube skin and process gas temperature, (c) outer wall heat flux and (d) total pressure for the ZoneFlow™ and the reference pellets reactors, along the dimensionless axial coordinate. The mixture feed composition is close to the equilibrium composition at the given feed temperature, so that the gas has to be heated in the first centimeters before reactions proceed. Despite the lower amount of catalyst in the ZoneFlow™ reactor, exit CH_4 and CO_2 conversions close to those with the reference pellets are obtained. The rapid increase of the temperature and of the CH_4 conversion in the first part of the ZoneFlow™ reactor is remarkable. The exit gas temperature is also significantly higher and the pressure drop significantly lower than with the reference pellets. Note that with the imposed conditions, the equilibrium composition does not change much above a certain temperature so that about the same methane conversion can be reached at lower exit gas temperature.

Heat transfer limitations are particularly pronounced in the first part of the reactor where the reaction rates are intrinsically high. In this region the methane conversion benefits most from the improved heat transfer in the ZoneFlow™ reactor. In the second part of the ZoneFlow™ reactor, as reactants are consumed and equilibrium is approached, reaction rates decrease and the improved heat transfer leads mostly to an increased process gas temperature. The available GSA (geometric surface area) and interfacial mass transfer limitations leading to low reactant concentrations on the catalyst surface contribute to reduced performance in terms of methane conversion in the second part of the reactor.

The improved heat transfer offered by the ZoneFlow™ reactor is reflected in the calculated heat flux profile in the first part of the reactor, in combination with a lower tube skin temperature (Figure 12(b)-(c)), showing significantly higher heat fluxes than with the reference pellets. The contribution of radiative heat transfer in the ZoneFlow™ reactor remains important, this mechanism representing around 35% of the total heat transferred to the process gas. It also explains that interfacial mass transfer limitations are stronger than interfacial heat transfer limitations. The blades coated with catalyst receive heat directly from the reactor tube wall through radiation. This is illustrated in Figure 12 showing profiles of (e) the methane mole fraction and (f) of the gas phase temperature at mid-height in the reactor along the dimensionless radial position in the annulus section, r^*. In the vicinity of the blades, interfacial heat transfer limitations result in a ΔT of 3 to 10 K depending on the axial position. Gradients in the radial direction are generally small, with the steepest temperature gradient in the near-reactor tube wall region (ΔT of 10 to 200 K depending on the axial position).

Figure 13 evaluates the risk of coke formation in the ZoneFlow™ reactor. Figure 13(a) shows axial profiles of the cross sectional averaged coke formation and gasification reaction rates and of the net rate of coke formation. A more detailed picture is given in Figure 13(b) showing contour plots of these reaction rates on the blades coated with catalyst in the inlet section of the reactor, where coke formation is typically to be feared most. Under the given conditions, throughout the reactor coke is formed by methane cracking, but is gasified by steam as soon as formed. The negative net rate of coke formation indicates no coke formation is to be feared [45–48].

4.3 Hybrid ZoneFlow™ - pellets reactor design

To optimize use of the heat made available by the high heat transfer performance of the ZoneFlow™ reactor for the conversion of methane, a hybrid ZoneFlow™ - pellets reactor design was considered. Figure 14 shows simulations using the ZoneFlow™ structure in the first three quarters of reactor length and conventional pellets in the last quarter. The potential increase in throughput is demonstrated by comparing the performance of a conventional pellets reactor at a feed flow rate of 399 Nm^3/h with that of a ZoneFlow™ reactor and of the hybrid ZoneFlow™ - pellets reactor at a feed flow rate of 500 Nm^3/h. Using the hybrid reactor allows increasing the throughput to 500 Nm^3/h while keeping the methane conversion and the process gas exit temperature at values very close to those obtained with the conventional pellets reactor at 399 Nm^3/h (Figure 14(a)). The maximum tube skin temperature can also be kept lower, despite the higher heat flux (Figure 14(b)). Furthermore, the pressure drop with the hybrid reactor at 500 Nm^3/h is similar to the pressure drop with the pellets reactor at 399 Nm^3/h. This is critical for recycle or closed loop systems, especially at low operating pressure. The process gas temperature profile and pressure drop illustrate how advantage can be taken from using the high heat transfer-low pressure drop ZoneFlow™ structure in the main part of the reactor, followed by a short packed bed of conventional pellets to rapidly consume the heat made available and maximize methane conversion.

Conclusions

The use of a thin coating structured ZoneFlow™ reactor for methane bi-reforming was studied by means of detailed multi-scale modeling and simulation. Scale-

bridging strategies include the use of Langmuir-Hinshelwood Hougen-Watson type reaction rate equations based on a detailed description of the reaction mechanism and the rate determining step theory, a pseudo-continuum description of the porous and tortuous catalyst layer and Reynolds-averaging of the 3D transport equations with the introduction of effective transport properties and a turbulence model to account for the effects of turbulence. Radiative heat transfer and thermal conduction in the reactor tube and in the reactor internals coated with catalyst were accounted for. Previously and independently determined model parameters for the intrinsic reaction kinetics and the catalyst layer structure were used as such, whereas the CFD turbulence model parameters were determined from cold flow pressure drop tests in a wide flow rate range. The coupled CFD-reaction model was validated using low-pressure methane bi-reforming pilot plant data.

The ZoneFlow™ reactor was found to significantly increase the catalyst effectiveness, improve the heat transfer and reduce the pressure drop. The latter is critical for processes that mix recycle gas with fresh methane feed, especially when operating low pressure and/or aiming at capacity increase. The simulations under typical commercial conditions show that advantage of improved heat transfer by the ZoneFlow™ structure in terms of methane conversion can mostly be taken in the first part of the reactor where reaction rates are intrinsically high. In the last part of the reactor, observed reaction rates are lower, also due to interfacial mass transfer limitations. Simulations with a hybrid reactor design show the advantage of combining a ZoneFlow™ structure in the first part of the reactor with a conventional packed bed of pellets in the last part of the reactor. The simulations demonstrate that a 25% increase in throughput is possible, without increasing the pressure drop or the maximum tube skin temperature and maintaining the exit process gas temperature

and methane conversion at their target values.

Acknowledgments

This work was financially supported by ZoneFlow™ Reactor Technologies, LLC. Computational resources have been provided by the Consortium des Équipements de Calcul Intensif (CECI), funded by the Fonds de la Recherche Scientifique de Belgique (F.R.S-FNRS) under Grant No.2.5020.11 and by the Walloon Region.

References

[1] X.E. Verykios, Catalytic dry reforming of natural gas for the production of chemicals and hydrogen, Int. J. Hydrogen Energ., 28 (2003) 1045-1063. https://doi.org/10.1016/S0360-3199(02)00215-X.

[2] J.D. Medrano-Garcia, R. Ruiz-Femenia, J.A. Caballero, Optimal carbon dioxide and hydrogen utilization in carbon monoxide production, J. CO2. Util, 34 (2019) 215-230. https://doi.org/10.1016/j.jcou.2019.05.005.

[3] D. Pakhare, J. Spivey, A review of dry (CO_2) reforming of methane over noble metal catalysts, Chem. Soc. Rev., 43 (2014) 7813-7837. https://doi.org/10.1039/C3CS60395D.

[4] N. Kumar, M. Shojaee, J.J. Spivey, Catalytic bi-reforming of methane: from greenhouse gases to syngas, Curr. Opin. Chem. Eng. 9 (2015) 8-15. https://doi.org/10.1016/j.coche.2015.07.003.

[5] G.A. Olah, A. Goeppert, M. Czaun, G.K.S. Prakash, Bi-reforming of Methane from Any Source with Steam and Carbon Dioxide Exclusively to Metgas ($CO-2H_2$) for Methanol and Hydrocarbon Synthesis, J. Am. Chem. Soc., 135(2) (2013) 648-650. https://doi.org/10.1021/ja311796n.

[6] N. Kumar, A. Roy, Z. Wang, E.M. L'Abbate, D. Haynes, D. Shekhawat, J.J. Spivey, Bi-reforming of methane on Ni-based pyrochlore catalyst, Appl. Catal. A: Gen. 517 (2016) 211-216. https://doi.org/10.1016/j.apcata.2016.03.016.

[7] M.M. Danilova, Z.A. Fedorova, V.I. Zaikovskii, A.V. Porsin, V.A. Kirillov, T.A. Krieger, Porous nickel-based catalysts for combined steam and carbon dioxide reforming of methane, Appl. Catal. B-Environ., 147 (2014) 858-863. https://doi.org/10.1039/C4CY01614A.

[8] T. Stroud, T.J. Smith, E. Le Saché, J.L. Santos, M.A. Centeno, H. Arellano-Garcia, J.A. Odriozola, T.R. Reina, Chemical CO_2 recycling via dry and bi reforming of methane using Ni-Sn/Al_2O_3 and Ni-Sn/CeO_2-Al_2O_3 catalysts, Appl. Catal. B-Environ., 224 (2018) 125-135. https://doi.org/10.1016/j.apcatb.2017.10.047.

[9] T. Ji Siang, L. Giang Bach, S. Singh, Q. Duc Truong, V.T. Thanh Ho, N.H. Huy Phuc, F. Alenazey, D.-V. N. Vo, Methane bi-reforming over boron-doped Ni/SBA-15 catalyst: Longevity evaluation, Int. J. Hydrogen Energ., 44 (2019) 20839-20850. https://doi.org/10.1016/j.ijhydene.2018.06.123.

[10] G. Mallikarjun, T.V. Sagar, S. Swapna, N. Raju, P. Chandrashekar, N. Lingaiah, Hydrogen rich syngas production by bi-reforming of methane with CO_2 over Ni supported on CeO_2-SrO mixed oxide catalysts, Catal. Today. https://doi.org/10.1016/j.cattod.2020.01.005.

[11] A. Stankiewicz, J.A. Moulijn, Re-Engineering the Chemical Processing Plant - Process Intensification, CRC Press, 2003.

[12] J.G. Xu, G.F. Froment, Methane steam reforming: II. Diffusional limitations and reactor simulation, AIChE J., 35 (1989) 97-103. https://doi.org/10.1002/aic.690350110.

[13] A. Chettouf, J.P. Den Breejen, R.J. Dogterom, M.S.H. Fleys, A structured catalyst for use in the Fischer-Tropsch process, Patent publ. no. US2017/0106354 A1, 2017.

[14] C.P. Rodrigues, E. Kraleva, H. Ehrich, F.B. Noronha, Structured Reactors as an Alternative to Fixed-bed Reactors: Influence of catalyst preparation methodology on the partial oxidation of ethanol, Catal. Today, 273 (2016) 12-24. https://doi.org/10.1016/j.cattod.2016.02.061.

[15] R. Balzarotti, M. Ambrosetti, A. Beretta, G. Groppi, E. Tronconi, Investigation of packed conductive foams as a novel reactor configuration for methane steam reforming, Chem. Eng. J. (2019). https://doi.org/10.1016/j.cej.2019.123494.

[16] M. Basin, D. Gary, W. Whittenberger, J. Shah, Increased steam methane reformer throughput: Switching to a foil based catalyst technology raised throughput substantially for a hydrogen producer, www.digitalrefining.com/article/1001360, 5 pages, 2017.

[17] J.J. Feinstein, Reactor with primary and secondary channels, patent publ. no. EP1773492 (A2), 2007.

[18] ZoneFlow™ Reactors - Structured Catalyst for Steam Methane Reforming, http://www.zoneflowtech.com, 2007.

[19] A.G. Dixon, M. Nijemeisland, CFD as a design tool for fixed-bed reactors, Ind. Eng. Chem. Res. 40 (2001) 5246-5252. https://doi.org/10.1021/ie001035a.

[20] A.G. Dixon, M.E. Taskin, E.H. Stitt, M. Nijemeisland, 3D CFD simulations of steam reforming with resolved intraparticle reaction and gradients, Chem. Eng. Sci. 62 (2007) 4963-4966. https://doi.org/10.1016/j.ces.2006.11.052.

[21] M.Behnam, A.G. Dixon, P.M. Wright, M. Nijemeisland, E.H. Stitt, Comparison of CFD simulations to experiment under methane steam reforming reacting conditions, Chem. Eng. J. 1 (2012) 690-700. https://doi.org/10.1016/j.cej.2012.07.038.

[22] G.D. Wehinger, T. Eppinger, M. Kraume, Detailed numerical simulations of catalytic fixed-bed reactors: Heterogeneous dry reforming of methane, Chem. Eng. Sci. 122 (2015) 197-209. https://doi.org/10.1016/j.ces.2014.09.007.

[23] A.G. Dixon, M.E. Taskin, M. Jijemeisland, E.H. Stitt, Wall-to-particle heat transfer in steam reformer tubes: CFD comparison of catalyst particles, Chem.

Eng. Sci. 63 (2008) 2219-2224. https://doi.org/10.1016/j.ces.2008.01.017.

[24] A.G. Dixon, CFD study of effect of inclination angle on transport and reaction in hollow cylinder catalysts, Chem. Eng. Res. Des. 92 (2014) 1279-1295. https://doi.org/10.1016/j.cherd.2013.11.018.

[25] A.G. Dixon, Local transport and reaction rates in a fixed bed reactor tube: Endothermic steam methane reforming, Chem. Eng. Sci. 168 (2017) 156-177. https://doi.org/10.1016/j.ces.2017.04.039.

[26] G.D. Wehinger, F. Klippel, M. Kraume, Modeling pore processes for particle-resolved CFD simulations of catalytic fixed-bed reactors, Comput. Chem. Eng. 101 (2017) 11-22. https://doi.org/10.1016/j.compchemeng.2017.02.029.

[27] G.D. Wehinger, S. Flaischlen, Computational Fluid Dynamics Modeling of Radiation in a Steam Methane Reforming Fixed-Bed Reactor, Ind. Eng. Chem. Res. 58 (2019) 14410-14423. https://doi.org/10.1021/acs.iecr.9b01265.

[28] A. Castedo, I. Uriz, L. Soler, L.M. Gandia, J. Llorca, Kinetic analysis and CFD simulations of the photocatalytic production of hydrogen in silicone microreactors from water-ethanol mixtures, Appl. Catal. B-Environ., 203 (2017) 210-217. https://doi.org/10.1016/j.apcatb.2016.10.022.

[29] B. Sawatmongkhon, A. Tsolakis, K. Theinnoi, A.P.E. York, P.J. Millington, R.R. Rajaram, Microkinetic modelling for selective catalytic reduction (SCR) of NOx by propane in a silver-based automotive catalytic converter, Appl. Catal. B-Environ., 111-112 (2012) 165-177. https://doi.org/10.1016/j.apcatb.2011.09.031.

[30] R. Ma, B. Castro-Dominguez, A.G. Dixon, Y.H. Ma, CFD study of heat and mass transfer in ethanol steam reforming in a cat-

alytic membrane reactor, Int. J. Hydrogen. Energ. 43 (2018) 7662-7674. https://doi.org/10.1016/j.ijhydene.2017.08.173.

[31] J. De Wilde, G.F. Froment, Computational fluid dynamics in chemical reactor analysis and design. Application to the ZoneFlow™ reactor for methane steam reforming, Fuel, 100 (2012) 46-56. https://doi.org/10.1016/j.fuel.2011.08.068.

[32] J. De Wilde, G.F. Froment, Modeling of Dual-Zone Structured Reactors for Natural Gas Steam Reforming, Ind. Eng. Chem. Res., 52 (2013) 14055-14065. https://doi.org/10.1021/ie401476s.

[33] H.S. Bengaard, J.K. Norskov, J. Sehested, B.S. Clausen, L.P. Nielsen, A.M. Molenbroek, J.R. Rostrup-Nielsen, Steam Reforming and Graphite Formation on Ni Catalysts, J. Catal. 209 (2002) 365-384. https://doi.org/10.1006/jcat.2002.3579.

[34] G. Jones, J.G. Jakobsen, S.S. Shim, J. Kleis, M.P. Andersson, J. Rossmeisl, F. Abild-Pedersen, T. Bligaard, S. Helveg, B. Hinnemann, J.R. Rostrup-Nielsen, E. Chorkendorff, J. Sehested, J.K. Norskov, First principles calculations and experimental insight into methane steam reforming over transition metal catalysts, J. Catal. 259 (2008) 147-160. https://doi.org/10.1016/j.jcat.2008.08.003.

[35] D.W. Blaylock, O. Teppei, W.H. Green, G.J.O. Beran, Computational investigation of thermochemistry and kinetics of steam methane reforming on Ni(111) under realistic conditions, J. Phys. Chem. C. 113 (2009) 4898-4908. https://doi.org/10.1021/jp806527q.

[36] Y. Yoon, H. Kim, J. Lee, Enhanced catalytic behavior of Ni alloys in steam methane reforming, J. Power Sources 359 (2017) 450-457. https://doi.org/10.1016/j.jpowsour.2017.05.076.

[37] S. Kolitcheff, E. Jolimaitre, A. Hugon, J. Verstraete, P.-L. Carrette, M. Tayakout-Fayolle, Tortuosity of mesoporous alumina catalyst supports: influence of the pore network organization, Microporous Mesoporous Mater. 248 (2017) 91-98. https://doi.org/10.1016/j.micromeso.2017.04.010.

[38] B.E. Launder, D.B. Spalding, The Numerical Computation of Turbulent Flows. Comput Methods Appl. Mech. Eng., 3 (1974) 269-289. https://doi.org/10.1016/0045-7825(74)90029-2.

[39] B.E. Launder, D.B. Spalding, Lectures in Mathematical Models of Turbulence, Academic Press, London, England, 1972.

[40] V.A. Durante, R. Gill, A. Davis, E.C. Soltani, Metal-Supported Catalyst Structures and Processes for Manufacturing the Same, U.S. Patent 9, US 2016/0354767 A1 (2016).

[41] A. Donazzi, A. Beretta, G. Groppi, P. Forzatti, Catalytic partial oxidation of methane over a 4% Rh/α-Al_2O_3 catalyst Part II: Role of CO_2 reforming, J. Catal. 255 (2008) 259-268. https://doi.org/10.1016/j.jcat.2008.02.010.

[42] F. Minette, M. Lugo-Pimenteel, D. Modroukas, A.W. Davis, R. Gill, M.J. Castaldi, J. De Wilde, Intrinsic kinetics of steam methane reforming on a thin, nanostructured and adherent Ni coating, Appl. Catal. B-Environ., 238 (2018) 184-197. https://doi.org/10.1016/j.apcatb.2018.07.015.

[43] M. Lugo, M. Castaldi, D. Modroukas, A.W. Davis, R. Gill, F. Minette, J. De Wilde, A new thin layered structural coating on a metal substrate for enhanced hydrogen production from steam methane reforming, American Institute of Chemical Engineers (AIChE), 2016 Annual meeting, San Francisco, CA, USA, November 17, 2016.

[44] Xu J.G., Froment G.F., Methane steam reforming, methanation and water-gas shift: I. Intrinsic kinetics, AIChE J., 35, 88, 1989. https://doi.org/10.1002/aic.690350109.

[45] J.-W. Snoeck, G.F. Froment, M. Fowles, Filamentous carbon formation and gasification: thermodynamics, driving force, nucleation, and steady-state growth, J. Catal. 169 (1997) 240-249. https://doi.org/10.1006/jcat.1997.1634.

[46] J.-W. Snoeck, G.F. Froment, M. Fowles, Kinetic study of the carbon filament formation by methane cracking on a nickel catalyst, J. Catal. 169 (1997b) 250-262. https://doi.org/10.1006/jcat.1997.1635.

[47] J.-W. Snoeck, G.F. Froment, M. Fowles, Steam/CO_2 reforming of methane. Carbon filament formation by the Boudouard reaction and gasification by CO_2, by H_2 and by steam: kinetic study. Ind. Eng. Chem. Res. 41 (2002) 4252-4265. https://doi.org/10.1021/ie010666h.

[48] J.-W. Snoeck, G.F. Froment, M. Fowles, Kinetic evaluation of carbon formation in steam/CO_2-natural gas reformers. Influence of the catalyst activity and alkalinity, Int. J. Chem. React. Eng., 1 (2002) A7. https://doi.org/10.2202/1542-6580.1001.

[49] Froment G.F., Bischoff K.B., De Wilde J., Chemical Reactor Analysis and Design, third ed., John Wiley & Sons, Inc, Hoboken, 2010.

[50] J. Beeckman, Mathematical description of heterogeneous materials, Chem. Eng. Sci. 45 (1990) 2603-2610. https://doi.org/10.1016/0009-2509(90)80148-8.

[51] K.A. Akanni, J.W. Evans, I.S. Abramson, Effective transport coefficient in heterogeneous media, Chem. Eng. Sci. 42 (1987) 1945-1954. https://doi.org/10.1016/0009-2509(87)80141-0.

[52] E.E. Petersen, Diffusion in a pore of varying cross section, AIChE J. 4 (1958) 343-345. https://doi.org/10.1002/aic.690040322.

[53] H.L. Weissberg, Effective diffusion coefficient in porous media, J. Appl. Phys. 34 (1963) 2636-2639. https://doi.org/10.1063/1.1729783.

[54] M.M. Tomadakis, S.V. Sotirchos, Transport properties of random arrays of freely overlapping cylinders with various orientation distributions, J. Chem. Phys. 98 (1993) 616-626. https://doi.org/10.1063/1.464604.

[55] Smith T.F., Shen Z.F., Friedman J.N., Evaluation of Coefficients for the Weighted Sum of Gray Gases Model, J. Heat Transfer, 104 (1982) 602-608. https://doi.org/10.1115/1.3245174.

[56] Siegel R., Howell J.R., Thermal Radiation Heat Transfer, Hemisphere Publishing Corporation, Washington DC., 1992.

[57] Hinze J., Turbulence. An introduction to its mechanism and theory, New York: McGraw-Hill, 1959.

[58] C. Jayatilleke, The influence of Prandtl Number and Surface Roughness on the Resistance of the Laminar Sublayer to Momentum and Heat Transfer. Prog. Heat Mass Transfer, 1 (1969) 193-321.

[59] S. Ergun. Fluid flow through packed columns. Chem. Eng. Prog, 48 (1952) 89-94.

[60] A.P. de Wasch, G.F. Froment, A two dimensional heterogeneous model for fixed bed catalytic reactors. Chem. Eng. Sci. 26 (1971) 629-634. https://doi.org/10.1016/0009-2509(71)86006-2.

Nomenclature

a	m^{-1}	Absorption coefficient
C_A	mol/m_g^3	Gas phase concentration of species A
$C_{A,s}^s$	mol/m_g^3	Surface concentration of species A
c_p	$J/kg.K$	Heat capacity at constant pressure
$C_{\epsilon i}$		Turbulence model parameter
C_μ		Turbulence model parameter
D_{AK}	m_g^2/s	Knudsen diffusivity of species A
D_{Am}	m_g^2/s	Molecular diffusivity of species A
$\mathcal{D}_{e,A}$	$m_g^3/m_{\text{cat}}.s$	Effective diffusivity of species A
D_t	$m_g^2.s$	Turbulent diffusivity in the gas
E_g	J/kg	Total (internal + kinetic) energy
g	m/s^2	Gravity acceleration
h_f	$W/m^2.K$	Interfacial heat transfer coefficient
ΔH_k	kJ/mol	Heat of reaction k
k	m^2/s^2	Turbulent kinetic energy
k_g	$m_g^3/m_i^2.s$	Interfacial mass transfer coefficient
n		Refractive index
P	bar	Total pressure
P_e	bar	Effective mean pressure
p_A	bar	Partial pressure of species A
Pr		Prandtl number
Pr_t		Turbulent Prandtl number
R	$J/mol.K$	Universal gas constant

r	m	Radial position coordinate or radius
r^*		Dimensionless radial coordinate in the reactor
r_k	$mol_A/kg_{\text{cat}}.s$	Intrinsic reaction rate of reaction k
Sc		Schmidt number
Sc_t		Turbulent Schmidt number
T_g	K	Gas temperature
T_{furnace}	K	Furnace temperature
T_s^s	K	Catalyst surface temperature
T_{w}	K	Tube wall temperature
u_i	m/s	i component of the velocity
x_i	m	Distance coordinate in direction i
y_A		Mole fraction of species A
z	m	Axial coordinate in the reactor

Greek letters

α_{Ak}		Stoechiometric coefficient of species A in global reaction k
α_i	$W/m^2.K$	Convective heat transfer coefficient, bed side
α_{rs}	$W/m^2.K$	Radiation coefficient for solid phase
α_{rv}	$W/m^2.K$	Radiation coefficient from void to void
α_u	$W/m^2.K$	Heat transfer coefficient, furnace side
α_w	$W/m^2.K$	Convective heat transfer coefficient in the vicinity of the wall
β	K^{-1}	Thermal expansion coefficient

δ_A		Expansion coefficient
δ_{ij}		Unit tensor, ij^{th} component
ε_s	m_g^3/m_{cat}^3	Catalyst porosity
ε_c		Emissivity of the catalyst material
ε_w		Emissivity of the wall material
ϵ	m^2/s^3	Turbulent dissipation rate
ζ	m	Coordinate in the catalyst coating
η_i		Catalyst effectiveness factor for reaction i
κ		von Karman constant, 0.42
λ_e	$W/m.K$	Effective conductivity
λ_{er}	$W/m.K$	Effective thermal conductivity in a packed bed, in the radial direction
λ_g	$W/m.K$	Gas thermal conductivity
λ_r	$W/m.K$	Radiative thermal conductivity
λ_s	$W/m.K$	Solid thermal conductivity
λ_t	$W/m.K$	Turbulent thermal conductivity
μ	$Pa.s$	Viscosity
μ_e	$Pa.s$	Effective viscosity
μ_t	$Pa.s$	Turbulent viscosity
ξ		Dimensionless coordinate in the catalyst
ρ_g	kg_g/m_g^3	Gas density
ρ_s	$kg_{\text{cat}}/m_{\text{cat}}^3$	Solid density
σ	$W/m^2.K^4$	Stefan-Boltzmann constant, 5.670367×10^{-8}
$\sigma_{\epsilon/k}$		Prandtl number for ϵ/k
τ		Catalyst tortuosity

τ_{ij}	$kg/m.s^2$	Shear stress tensor, ij^{th} component

Tables

Parameter	Value	Parameter	Value
k_1	$2.69 \times 10^{16} \exp\left(\frac{-226400}{RT}\right)$	k_o^-	$1.33 \times 10^{-6} \exp\left(\frac{75955}{RT}\right)$
k_2	$1.95 \times 10^{9} \exp\left(\frac{-67130}{RT}\right)$	$k_o^{+\prime}$	$1.67 \times 10^{9} \exp\left(\frac{-148916}{RT}\right)$
k_3	$3.44 \times 10^{15} \exp\left(\frac{-210400}{RT}\right)$	$\widetilde{K}_{CH_4}$	0.1099
K_1	$10^{\left(\frac{-11650}{T}+13.076\right)}$	K_M^*	$\exp\left(\frac{142.5}{R}\right) \exp\left(\frac{-123226}{RT}\right)$
K_2	$10^{\left(\frac{1910}{T}-1.764\right)}$	K_{O,H_2O}	$1.7372 \times 10^{4} \exp\left(\frac{-60615}{RT}\right)$
K_3	$10^{\left(\frac{-9740}{T}+11.312\right)}$	K_r''	$2.51893 \times 10^{5} \exp\left(\frac{-95489}{RT}\right)$
K_{CO}	$8.23 \times 10^{-5} \exp\left(\frac{70650}{RT}\right)$	ΔH_1	224 000 (at 948 K)
K_{H_2}	$6.12 \times 10^{-9} \exp\left(\frac{82900}{RT}\right)$	ΔH_2	−37 300 (at 948 K)
K_{CH_4}	$2.68 \times 10^{-4} \exp\left(\frac{38280}{RT}\right)$	ΔH_3	187 500 (at 948 K)
K_{H_2O}	$2.09 \times 10^{5} \exp\left(\frac{-88680}{RT}\right)$	ΔH_{c1}	74 870 (at 298 K)
k_M^+	$5.5619 \times 10^{4} \exp\left(\frac{-65053}{RT}\right)$	ΔH_{c2}	−131 325 (at 298 K)

Table 1 – Thermodynamic and rate constants for the rate equations for steam methane reforming on ASC catalyst (see Eqs. 1-4) for partial pressures expressed in bar and reaction rates in mol/kg_{cat}.h and for coke formation and gasification (see Eqs. 5-7) [42–48]) for partial pressures expressed in bar and reaction rates in kmol/m_i^2.h.

	Pilot scale		Commercial scale
Operating conditions	**Test 1**	**Test 2**	**Typical bi-reformer**
Pressure (bar)	2.5	2.5	2
Flow rate (Nm^3/h)	36.9	60.6	399, 500
Space velocity ($Nm^3/h/m_r^3$)	1198	1956	873, 1094
Feed gas composition (mol%)			
CH_4	17.67	17.58	17
H_2O	13.87	13.86	13
H_2	33.33	33.56	35
CO	17.21	16.99	19
CO_2	14.80	14.99	15
N_2	2.45	2.30	1
others (C_2H_6, C_3H_8)	0.68	0.73	/
Feed gas temperature (K)	884.05	882.55	853.15
Furnace temperature (K)	1358.15	1298.15	1323.15

Table 2 – Operating conditions in the methane bi-reforming pilot plant tests and as considered for typical commercial operation.

Test 1 - outlet concentrations (dry %)						
Species	Measured	Equilibrium at T_{exit} (1169K)	Simulated Rosseland model	Simulated Rosseland model No conduction	Simulated DO model	Simulated No radiation
CH_4	10.23	0.41	9.85	9.86	10.25	11.57
H_2	48.34	58.53	49.54	49.8	49.06	47.93
CO	28.92	36.28	28.76	28.75	28.71	27.16
CO_2	8.73	2.83	8.64	8.64	8.73	10.01
N_2	3.47	1.95	3.21	2.95	3.25	3.23
Test 2 - outlet concentrations (dry %)						
Species	Measured	Equilibrium at T_{exit} (1170K)	Simulated Rosseland model	Simulated Rosseland model No conduction	Simulated DO model	Simulated No radiation
CH_4	11.76	0.35	11.70	11.74	12.91	13.23
H_2	47.23	58.65	47.35	47.32	46.03	45.88
CO	26.93	36.32	26.89	26.86	26.3	25.44
CO_2	10.37	2.83	10.14	10.16	10.73	11.42
N_2	3.31	1.85	3.92	3.92	4.03	4.03

Table 3 – Simulations of the bi-reforming pilot plant tests using a ZoneFlow™ reactor. Comparison of the measured and simulated outlet compositions (on a dry basis) and sensitivity study of the contribution of radiative heat transfer using the Rosseland and the DO radiation models, and of thermal conduction in the reactor internals.

Simulated	**Pellets reactor 399 Nm^3/h**	**ZoneFlow™ reactor 399 Nm^3/h**	**Pellets reactor 500 Nm^3/h**	**ZoneFlow™ reactor 500 Nm^3/h**	**Hybrid ZoneFlow™ - pellets reactor 500 Nm^3/h**
Species (vol%)					
CH_4	1.14	1.11	1.85	2.03	0.88
H_2	54.13	54.37	53.25	53.27	55.71
CO	34.42	34.64	33.8	33.33	33.76
CO_2	3.36	3.21	3.82	4.24	3.01
H_2O	6.18	6.02	6.54	6.33	6.05
N_2	0.77	0.65	0.74	0.8	0.59
Outlet temperature (K)	1135.3	1291.5	1116.3	1265.5	1147.8
Pressure drop (mbar)	222.1	60.1	307.2	79.08	225.31

Table 4 – Comparison of the conventional pellets reactor performance with that of the ZoneFlow™ and the hybrid ZoneFlow™ - pellets reactors under typical commercial process conditions, assuming equal reaction kinetics for the catalyst, an imposed furnace temperature of 1323K and a feed flow rate of 399 or 500 Nm^3/h.

Figures

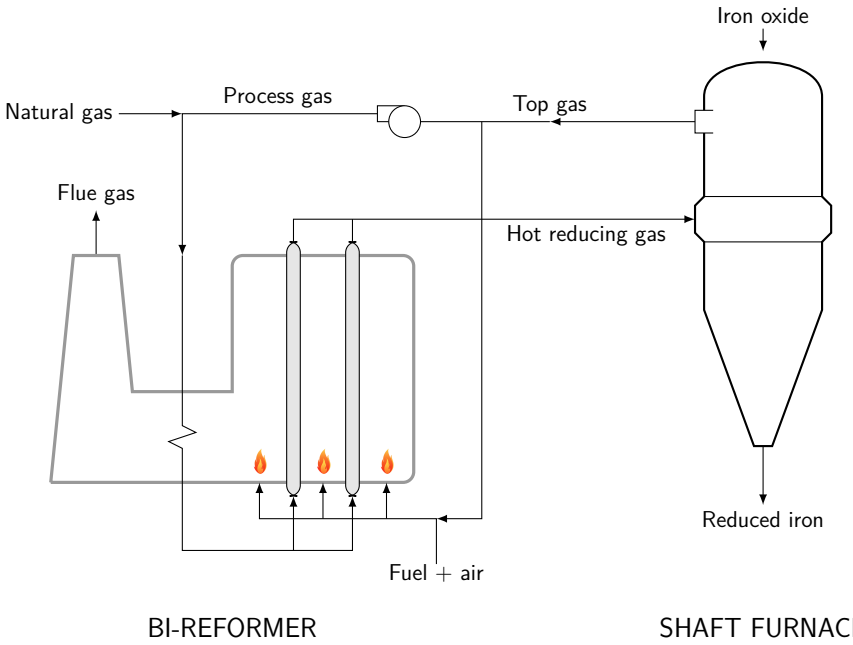

Figure 1 – Example of a low-pressure bi-reformer used in a closed-loop iron oxide reduction process.

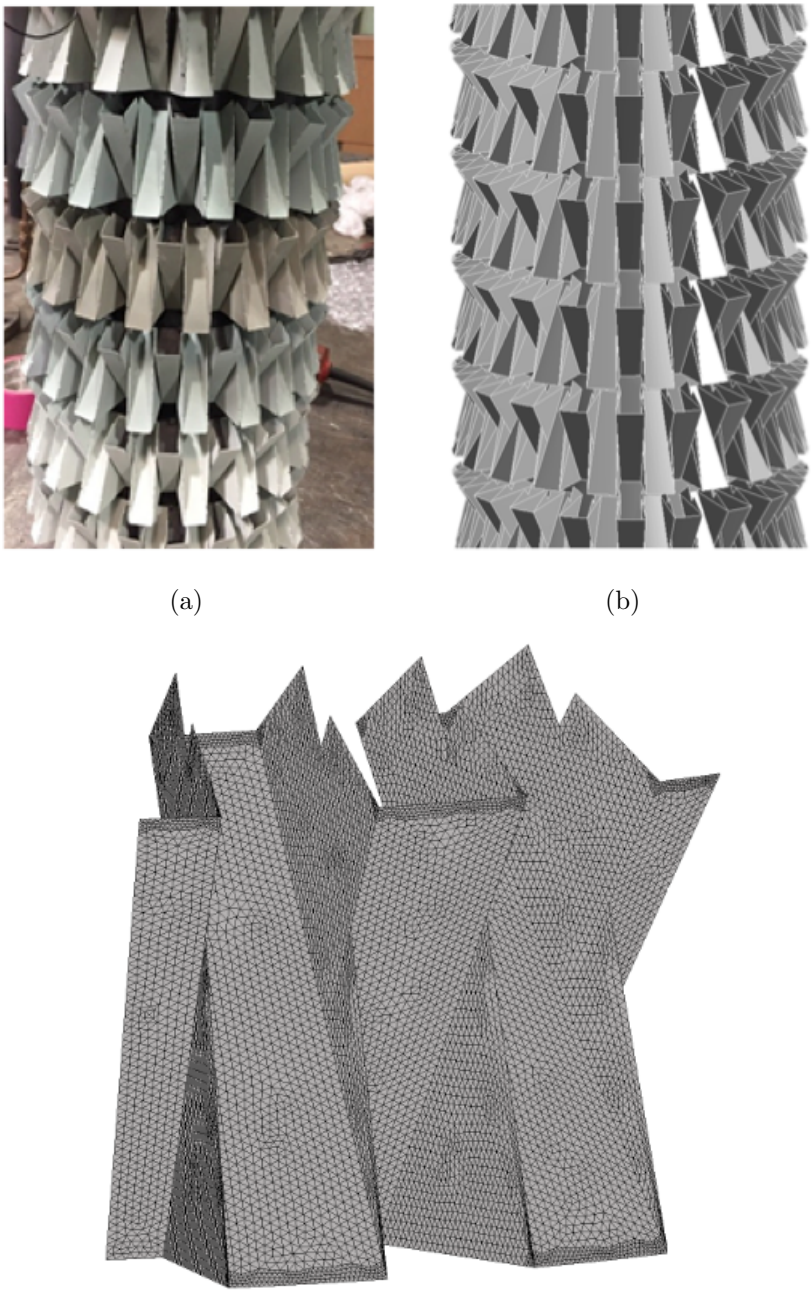

(a) (b)

(c)

Figure 2 – (a) ZoneFlow™ reactor casing as used in the bi-reforming pilot plant tests, (b) generated geometry for the CFD simulations and (c) visualization of the final mesh used in the simulations, with local grid refinement.

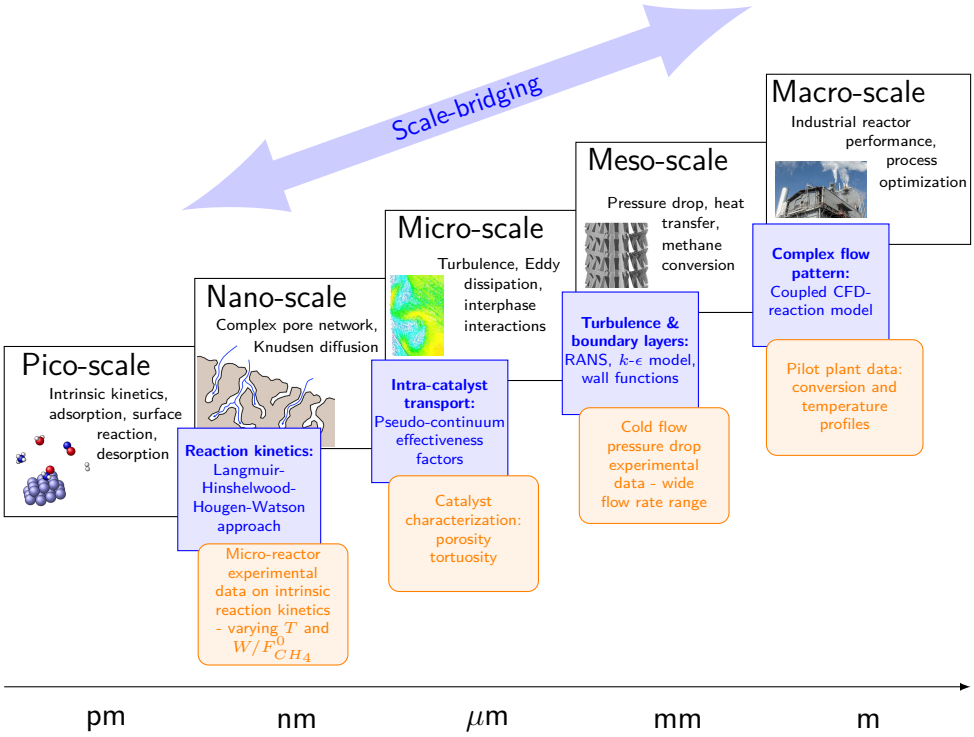

Figure 3 – Multi-scale modeling approach and scale-bridging strategies.

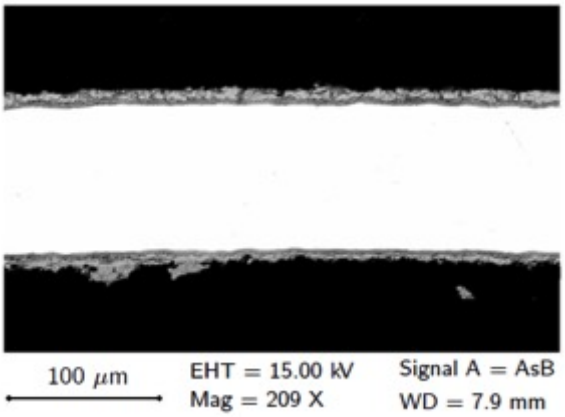

(a)

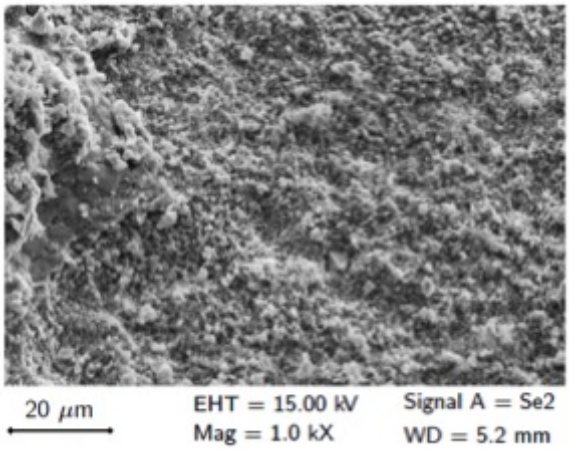

(b)

Figure 4 – SEM pictures of the Alloy Surfaces Co., Inc. (ASC) catalyst with a 100 μm support and a 10 μm Ni catalyst coating used in the bi-reforming pilot plant tests: (a) cross-section and (b) top view.

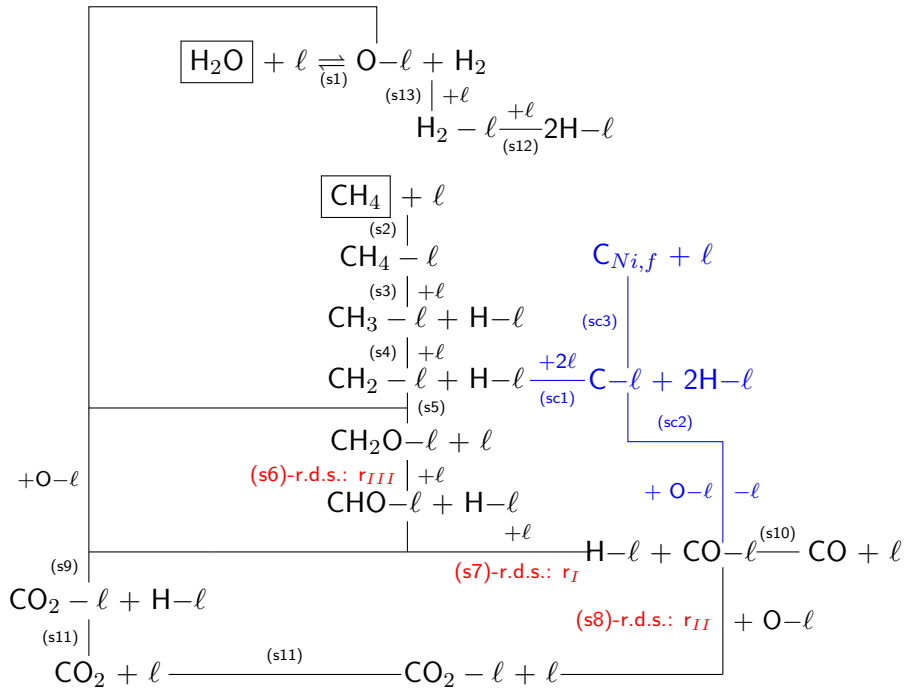

Figure 5 – Reaction mechanism and rate determining steps for steam methane reforming on an ASC catalyst and for coke formation (shown in blue). An active site is represented by ℓ. Adopted from [42–48].

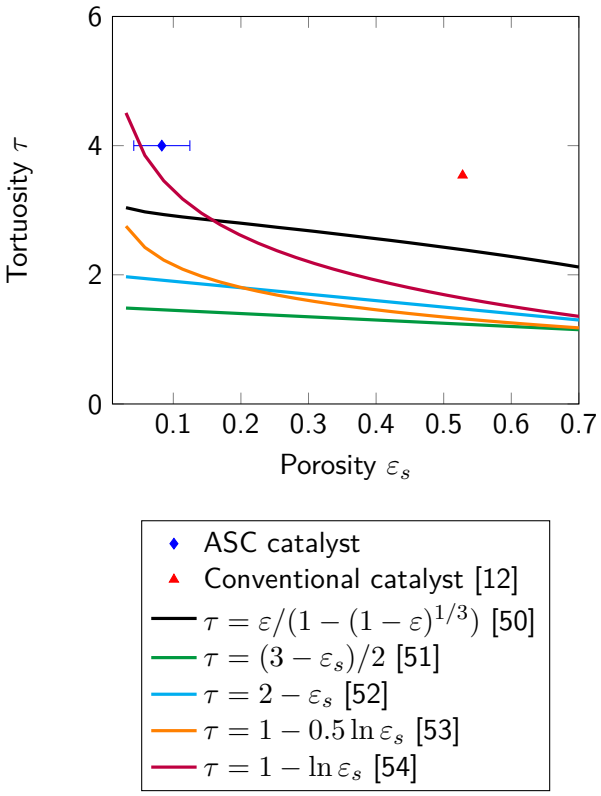

Figure 6 – Estimation of the catalyst tortuosity from the catalyst porosity applying the correlations of Beeckman (1990) [50], Akanni and Evans (1987) [51], Petersen (1958) [52], Weissberg (1963) [53] and Tomadakis and Sotirchos (1993) [54], tortuosity of the conventional catalyst experimentally measured by Xu and Froment (1989b) [12] and tortuosity used in this work for the ASC catalyst.

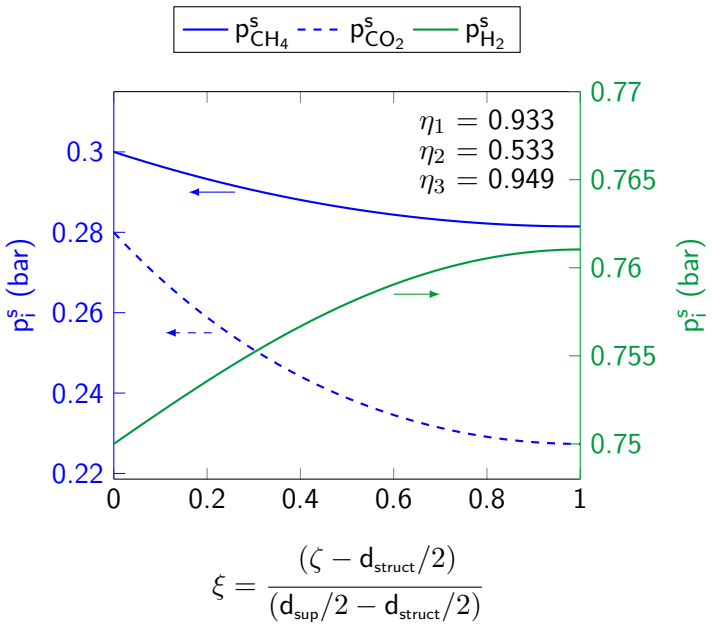

Figure 7 – Intra-catalyst species concentration profiles for typical commercial bi-reforming process conditions (T_s = 1023 K, P = 2 bar, y_{CH_4} = 0.15, y_{H_2O} = 0.125, y_{H_2} = 0.375, y_{CO} = 0.205, y_{CO_2} = 0.14) and corresponding catalyst effectiveness factors. Profiles of the CH_4, CO_2 and H_2 partial pressures versus the normalized intra-catalyst coordinate ξ.

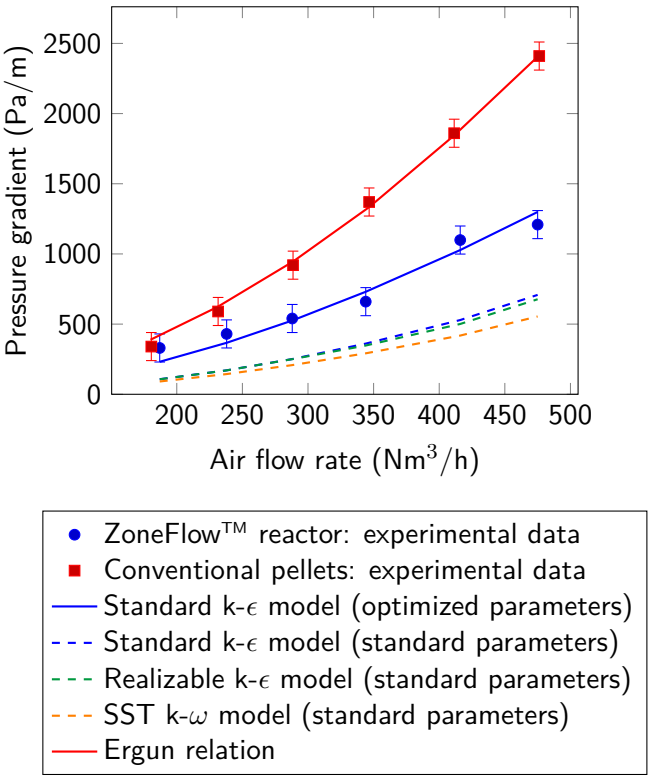

Figure 8 – Cold flow pressure drop tests for the optimization of the $k-\epsilon$ turbulence model parameters for the ZoneFlow™ reactor and for verification of the pellets reactor bed density. Measured versus calculated pressure gradient using the standard and realizable $k-\epsilon$ and the SST k-ω turbulence models with standard values of the parameters and using the standard k-ϵ turbulence model with optimized values of the parameters ($C_{\epsilon 1} = 0.8$, $C_{\epsilon 2} = 3.2$) for the ZoneFlow™ reactor, and using the Ergun relation for the pellets ($d_p = 1.29$ cm; $\varepsilon_b = 0.56$ m^3_g/m^3_{cat}).

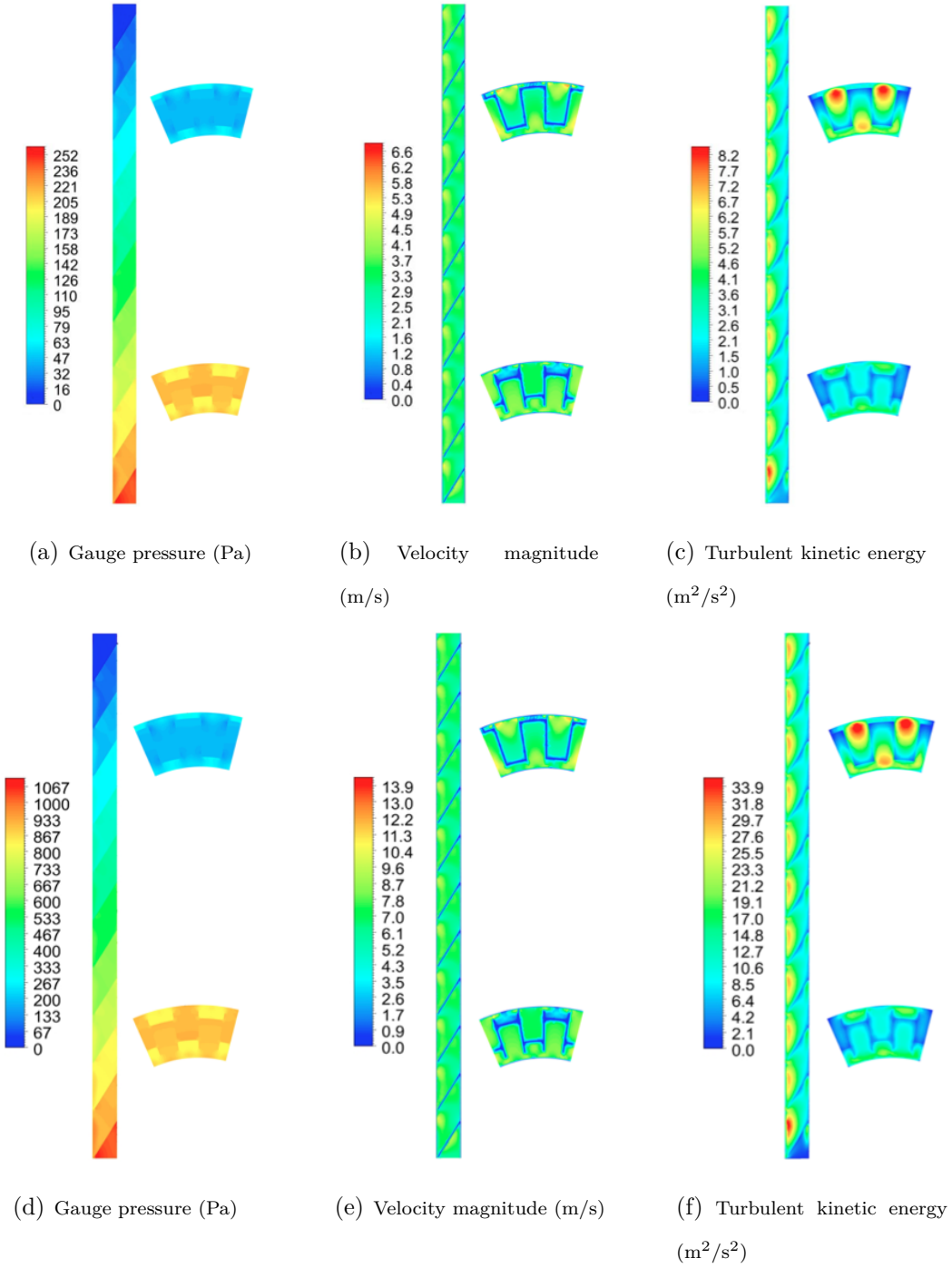

(a) Gauge pressure (Pa) (b) Velocity magnitude (m/s) (c) Turbulent kinetic energy (m^2/s^2)

(d) Gauge pressure (Pa) (e) Velocity magnitude (m/s) (f) Turbulent kinetic energy (m^2/s^2)

Figure 9 – Example of cold flow pressure drop test CFD simulations. Profiles of the (a)/(d) Gauge pressure (Pa), (b)/(e) velocity magnitude (m/s) and (c)/(f) turbulent kinetic energy (m^2/s^2) at the lowest ($F_{air} = 238$ Nm^3/h) and highest ($F_{air} = 475$ Nm^3/h) applied air flow rates. Cross-sections in the axial direction in a blades sector guiding the flow away from the wall and in the radial direction at z = 0.1 m and z = 0.7 m.

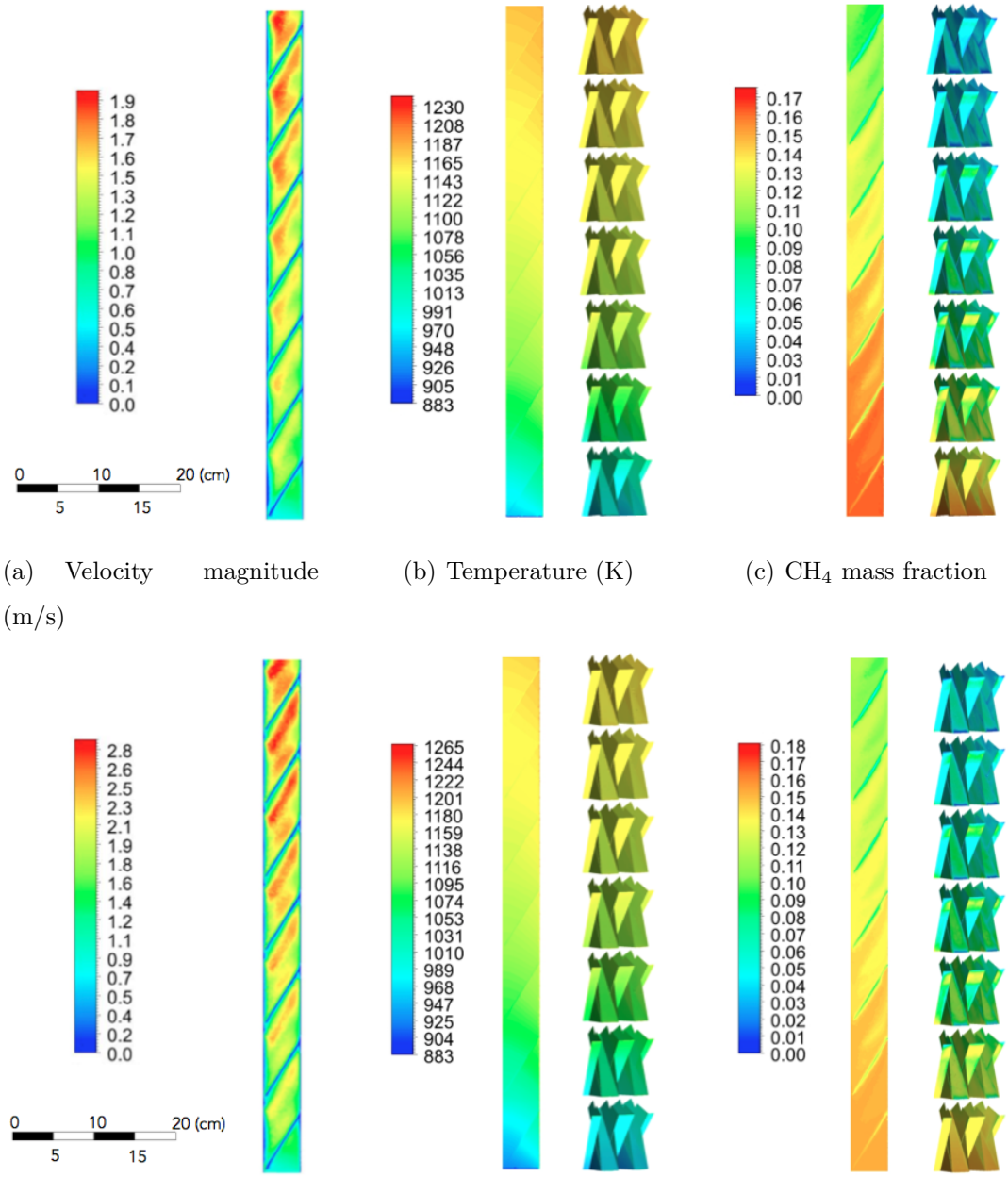

(a) Velocity magnitude (m/s) (b) Temperature (K) (c) CH_4 mass fraction

(d) Velocity magnitude (m/s) (e) Temperature (K) (f) CH_4 mass fraction

Figure 10 – Simulation of the methane bi-reforming pilot plant (a)-(c) test 1 and (d)-(f) test 2. Contour plots in a centrifugal blades sector of the (a) and (d) velocity magnitude (m/s), (b) and (e) gas phase and catalyst temperature (K), and (c) and (f) CH_4 mass fraction in the gas phase and at the catalyst surface.

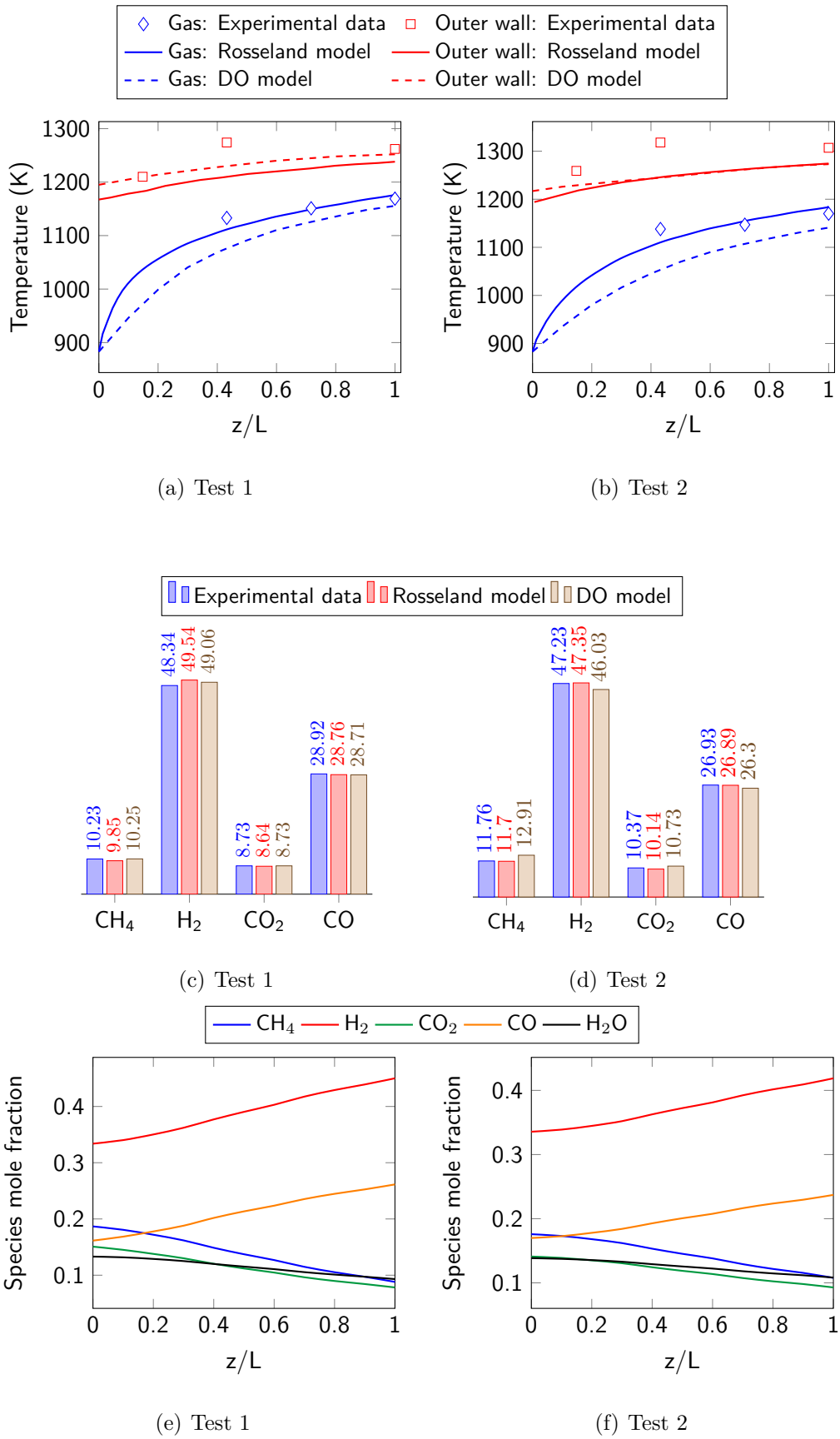

(a) Test 1 (b) Test 2

(c) Test 1 (d) Test 2

(e) Test 1 (f) Test 2

Figure 11 – Methane bi-reforming pilot plant tests. Comparison of (a)-(b) the measured and simulated gas and tube skin temperature profiles, (c)-(d) the measured and simulated exit dry concentrations using the Rosseland and the DO radiation models. (e)-(f) Simulated axial profiles of the species mole fractions.

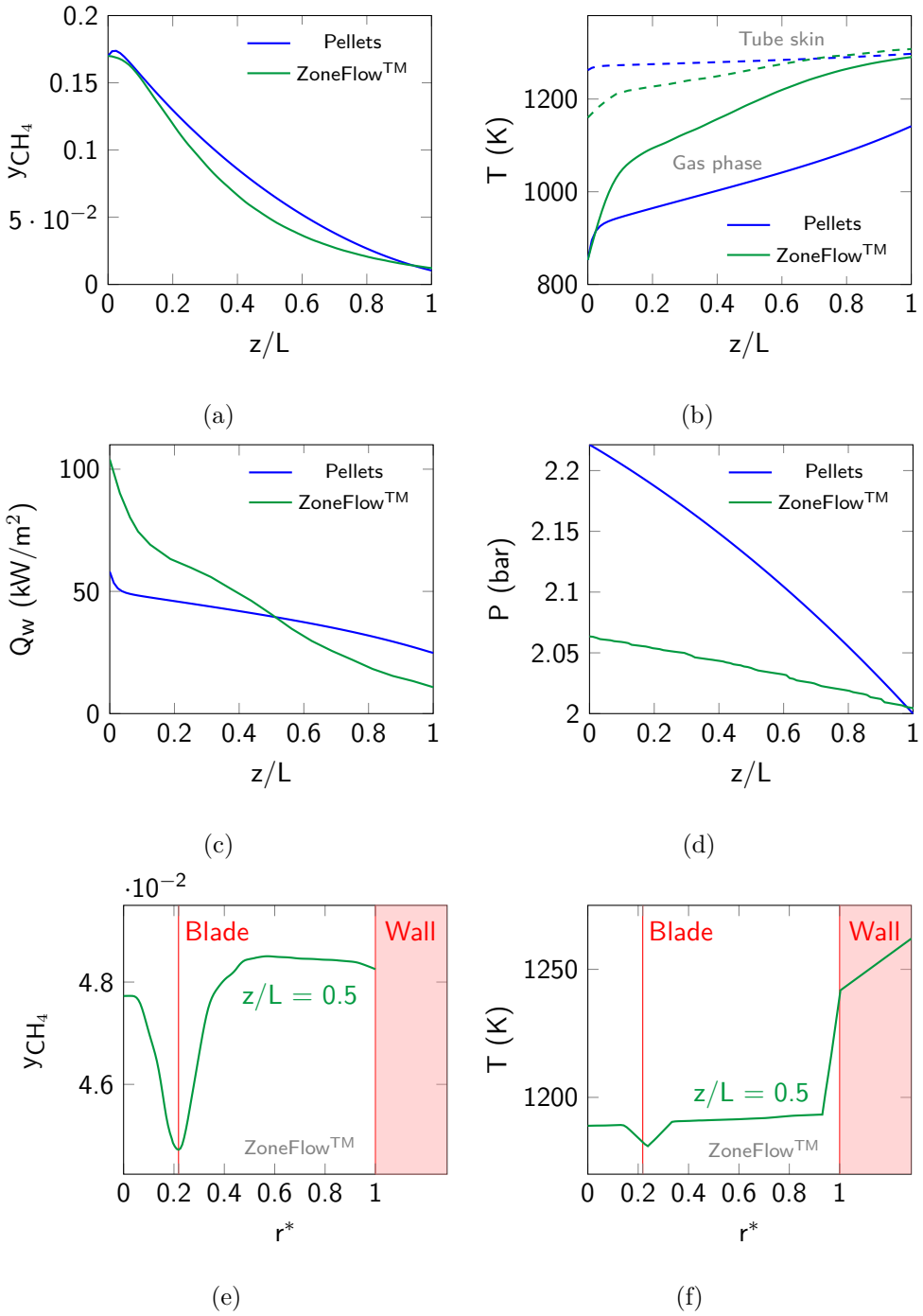

Figure 12 – Simulations under typical commercial low-pressure bi-reforming conditions with a feed flow rate of 399 Nm^3/h and an imposed constant furnace temperature of 1323K. Comparison between the ZoneFlow™ reactor and the reference pellets reactor. Normalized axial profiles of the (a) methane mole fraction, (b) process gas (solid lines) and tube skin (dashed lines) temperatures, (c) outer tube heat flux and (d) total pressure. Normalized radial profiles of the (e) methane mole fraction and (f) temperature at mid-height in the ZoneFlow™ reactor.

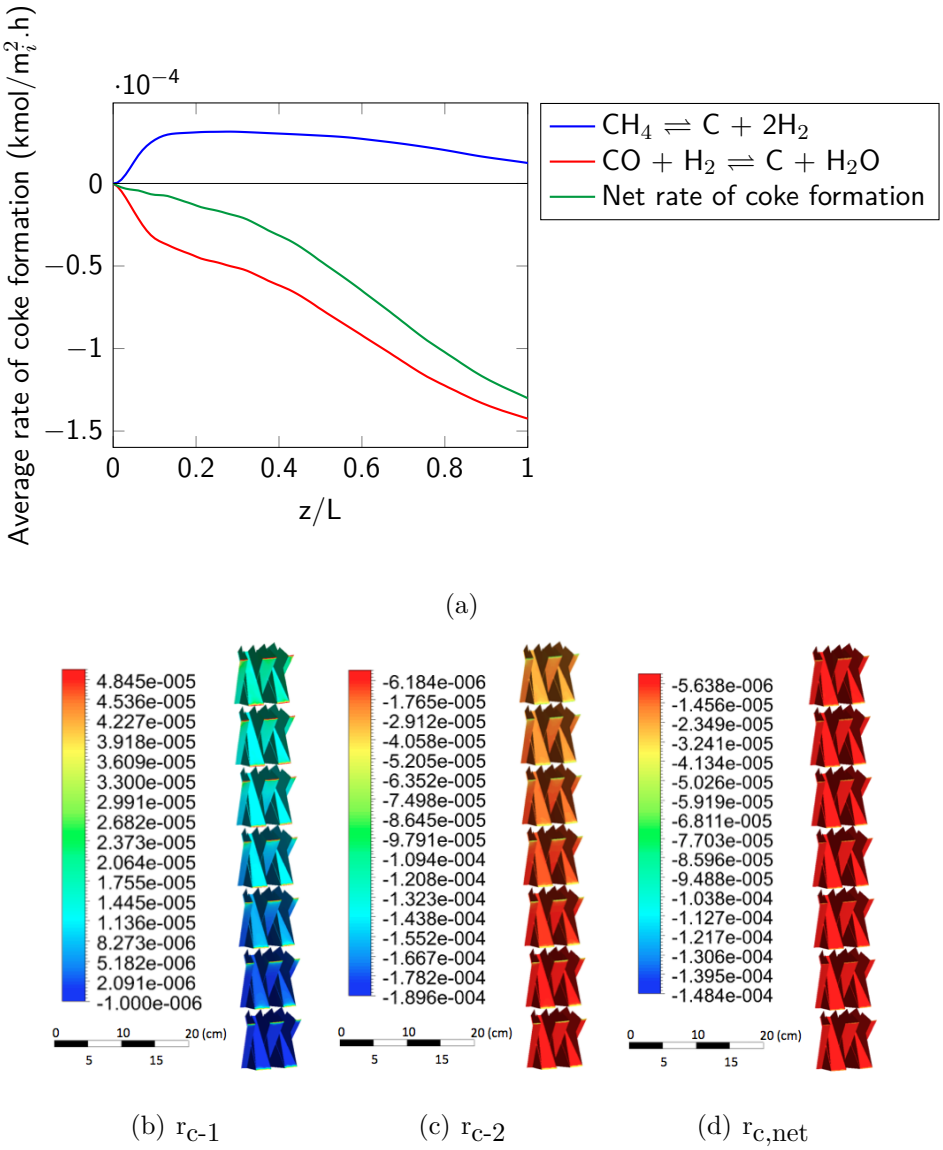

(a)

(b) $r_{c\text{-}1}$ (c) $r_{c\text{-}2}$ (d) $r_{c,net}$

Figure 13 – Coke formation analysis under typical commercial low-pressure bi-reforming conditions. Simulation with a feed flow rate of 399 Nm^3/h and an imposed constant furnace temperature of 1323 K using a ZoneFlow™ reactor. (a) Cross-section averaged rates of reaction C-1, C-2 and net rate of coke formation. Contour plots on the blades coated with catalyst of reactions (b) C-1, (c) C-2 and (d) net rate of coke formation in the inlet section of the reactor.

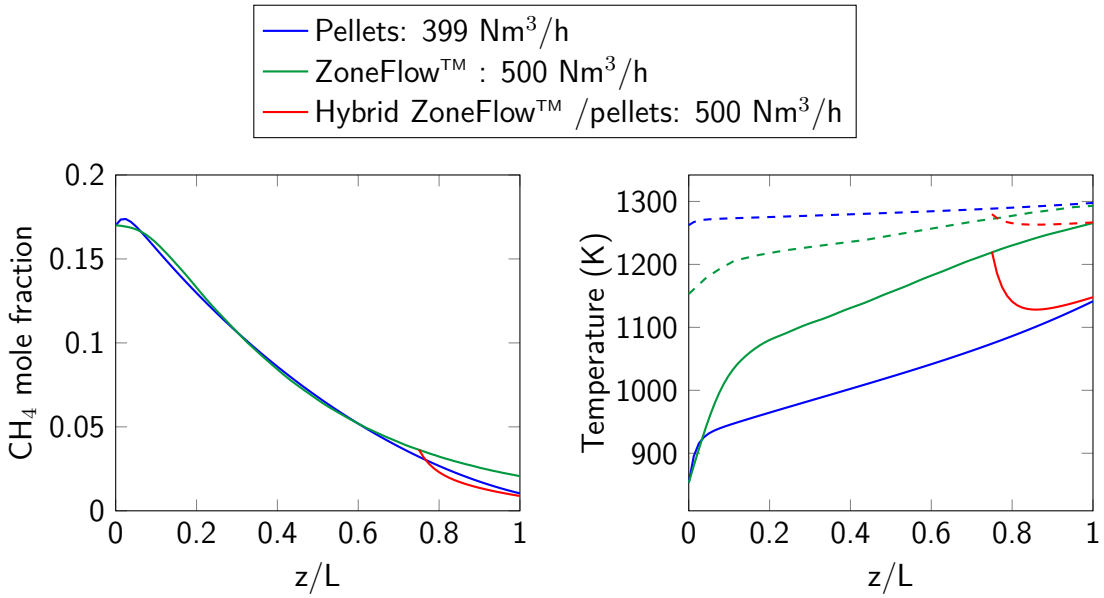

(a) (b)

Figure 14 – Increase in capacity using a hybrid ZoneFlow™ - pellets reactor. Comparison of a reference pellets reactor operating at 399 Nm^3/h with a ZoneFlow™ reactor and a hybrid ZoneFlow™ / pellets reactor, both operating at 500 Nm^3/h, with a constant temperature furnace of 1323K.